iScience

CellPress
REVIEWS

Review

Prussian Blue Analogs for Rechargeable Batteries

Baoqi Wang,[1] Yu Han,[2] Xiao Wang,[1] Naoufal Bahlawane,[3] Hongge Pan,[1] Mi Yan,[1] and Yinzhu Jiang[1,*]

SUMMARY

Non-lithium energy storage devices, especially sodium ion batteries, are drawing attention due to insufficient and uneven distribution of lithium resources. Prussian blue and its analogs (Prussian blue analogs [PBAs]), or hexacyanoferrates, are well-known since the 18th century and have been used for hydrogen storage, cancer therapy, biosensing, seawater desalination, and sewage treatment. Owing to their unique features, PBAs are receiving increasing interest in the field of energy storage, such as their high theoretical specific capacity, ease of synthesis, as well as low cost. In this review, a general summary and evaluation of the applications of PBAs for rechargeable batteries are given. After a brief review of the history of PBAs, their crystal structure, nomenclature, synthesis, and working principle in rechargeable batteries are discussed. Then, previous works classified based on the combination of insertion cations and transition metals are analyzed comprehensively. The review includes an outlook toward the further development of PBAs in electrochemical energy storage.

INTRODUCTION

There has been a revolutionary trend toward the use of clean energy, such as solar, wind, hydraulic, and tidal energy, instead of exhausting traditional fossil energy sources (Dunn et al., 2011). The intermittent nature of most renewable energies drives forward the development of advanced electric energy storage (EES) technologies for achieving constant electricity output. Lithium ion batteries (LIBs) have been successfully powering portable electronics and electric vehicles since the commercialization of LIBs in the early 1990s (Hwang et al., 2017). However, with the ever-increasing usage of LIBs, the insufficient and unevenly distributed lithium resources might impede their further applications, especially in the large-scale battery packs for stationary energy storage. Non-lithium rechargeable batteries are emerging as a low-cost alternative to LIBs in recent years, among which sodium ion batteries (SIBs) attracted the most attention due to the similar chemistry as LIBs (Qian et al., 2018). In spite of the lower specific charge of sodium relative to lithium, the worldwide abundance and low cost of sodium makes it superior to lithium in large-scale energy storage systems. Two primary kinds including aqueous and aprotic SIBs were intensively investigated in the past years. Modifying existing cathode materials used in LIBs, such as layered oxide materials, has become a logical thought because of the similar working principle of SIBs and LIBs (Paolella et al., 2017). Unfortunately, many highly performing cathode materials in LIBs are unable to bring up their refulgence into SIBs due to the much larger ion radius of sodium ion (Lu et al., 2012). Therefore synthesizing conceptually new materials for SIBs has become critically important for the advance of SIBs.

Prussian blue (PB) was first produced in the laboratory of Johann Conrad Dippel by mistake (Xu et al., 2017). The details about its production were kept secret until John Woodward reported its synthesis procedure in 1724. Subsequently, PB was used as a pigment in the 18th and 19th centuries. With further investigation, PB has been applied in more and more fields, such as hydrogen storage (Xu et al., 2017), biosensing (Karyakin et al., 1995), cancer therapy (Jia et al., 2015a), seawater desalination (Guo et al., 2017), and sewage treatment (Vipin et al., 2013). PB's potentials for energy storage were deeply delved for the past few years, as shown in Figure 1. PB allows multiple modifications of its chemical composition without breaking the overall crystal structure of the system. Substitutional and interstitial modifications of PB lead to a series of new compounds generally called Prussian blue analogs (PBAs). The rigid open framework and small interaction with interstitial cations make PBAs become remarkable emerging electrode materials for SIBs (Table 1).

PBAs were also introduced into secondary batteries employing cations other than sodium for charge transfer. Owing to the large interstitial sites of PBAs, which are capable of storage of almost all the alkali metals

[1]State Key Laboratory of Silicon Materials, Key Laboratory of Novel Materials for Information Technology of Zhejiang Province and School of Materials Science and Engineering, Zhejiang University, Hangzhou 310027, China

[2]State Key Laboratory of Advanced Transmission Technology, Global Energy Interconnection Research Institute Co. Ltd, Beijing 102211, China

[3]Material Research and Technology Department, Luxembourg Institute of Science and Technology, 41, rue du Brill, L-4422 Belvaux, Luxemburg

*Correspondence: yzjiang@zju.edu.cn

https://doi.org/10.1016/j.isci.2018.04.008

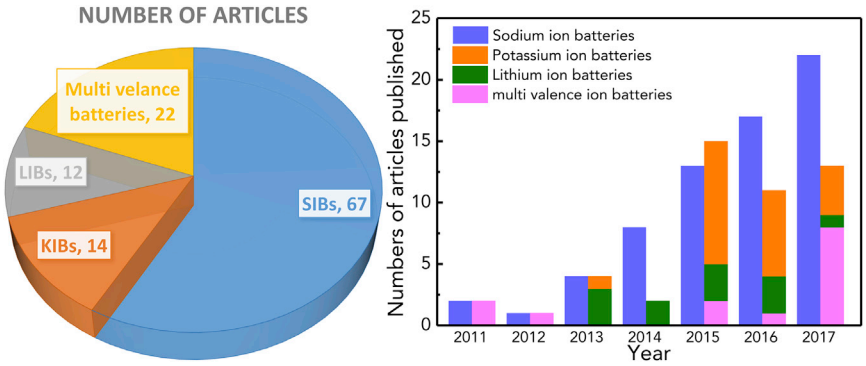

Figure 1. Number of Published Articles of Prussian Blue Analogs for Rechargeable Ion Batteries.

and even multivalence metals, such as Mg, Ca, Zn, and Al, PBAs have bright prospects for use in potassium ion batteries (KIBs), LIBs, and multivalence ion batteries.

In this article, a comprehensive review of PBAs' applications in secondary batteries, especially SIBs, is proposed. Recent progress in PBAs used as cathodes and anodes for secondary batteries is all-sided summarized and classified according to the types of batteries and transition metals. In retrospect of the developmental history of PBAs for secondary batteries, milestone works indicating key issues in promoting the performance of PBAs or providing brilliant ideas to overcome the barriers of development of PBAs are highlighted. This review aims at providing guidance toward further progress of PBAs for secondary batteries.

Crystal Structure, Nomenclature, and Working Principle

The generic formula of a PBA system can be roughly represented as $A_xM_{A_y}[M_B(CN)_6]_z\cdot nH_2O$, where M_A and M_B are usually Mn, Fe Co, Ni, Cu, or Zn, and A is usually Li, Na, or K. Although M_A and M_B can be the same transition metal and often be distinguished according to their valence states, the intrinsic difference between them is their spin states determined by the strength of ligands around the central ion. As can be seen in Figure 2A, high-spin (HS) M_A located in M_AN_6 octahedra and low-spin (LS) M_B located in M_BC_6 octahedra result from weak N-coordinated and strong C-coordinated crystal fields, respectively. These two kinds of octahedra are interconnected by C≡N bridges alternately forming a cubic open framework. On the basis of precursors and preparation conditions, M_A and M_B presented a variety of combination of valence states. However, since the space group symmetry usually corresponds to *Fm-3m* (typical crystal structures of PBAs are shown in Table 2), a random distribution of the $M_B(CN)_6$ vacancies is assumed. The number of these empty $M_B(CN)_6$ sites depends on the stoichiometry of the particular compound, which is related to the valences of the two metal ions M_A and M_B. For instance, the original PB $Fe_4[Fe(CN)_6]_3\cdot nH_2O$ (n = 6–14) is a typical mixed-valence compound, in which Fe^{HS} and Fe^{LS} ions are in the 3+ and 2 + oxidation states, respectively. Owing to the specific stoichiometry of this compound (3: 4 ratio of Fe^{2+} and Fe^{3+} sites), the charge neutrality implies a 25% vacancy of $[Fe^{II}(CN)_6]^{4-}$ clusters (Kumar et al., 2005). As shown in Figure 2B, the resulting octahedral cavities are occupied by H_2O molecules, called the coordinated water. Six water molecules are attached to six Fe^{HS} ions forming the corners of the octahedral cavity. Besides the coordinated water, the remaining water molecules called zeolitic water or interstitial water partially or fully occupy the eight possible 8c (1/4, 1/4, 1/4) sites of the unit cell. It is worth mentioning that the electrochemical energy storage in PBAs takes benefit from variable valence states of transition metals but requires vacant 8c sites for the insertion ions. The structure of the $Fe_4[Fe(CN)_6]_3\cdot nH_2O$, where $n \leq 14$, system was well studied by both X-ray and neutron diffraction techniques (Kumar et al., 2005; Lu et al., 2012; Widmann et al., 2002).

Two features of PBA structures are of high relevance for secondary energy storage materials:

- There are sufficiently large three-dimensional diffusion channels with weak interaction with the diffusing ion to facilitate its inward and outward transport.
- The $[M_B(CN)_6]^{4-}$ vacancies can be reduced by means of the synthesis process controlling to improve the crystallinity, which is essential for long-term cycling and high specific capacity.

Composition	Reversible Capacity in Na Cells (mAh g^{-1}) *	Average Working Voltage (V versus Na^+/Na)	Rate Performance	Cycle Life
$Na_{0.44}MnO_2$	113(50)	2.8	84% at 5 C	94%@20th
$Na_{0.85}Li_{0.17}Ni_{0.21}Mn_{0.64}O_2$	100	3.4	65% at 25C	98%@ 50th
O3-$NaNi_{0.5}Mn_{0.5}O_2$	125	2.8	84% at 1C	75% @ 50th
$NaNi_{1/3}Mn_{1/3}Co_{1/3}O_2$	120	2.8	67% at 1C	~100% @50th
P2-$Na_{2/3}Fe_{1/2}Mn_{1/2}O_2$	190(140)	2.75	70% at 1C	78% @30th
$FePO_4$	120(0)	2.6	68% at 0.5C	88% @ 50th
$Na_3V_2(PO_4)_3$	113	3.4	74% at 1C	95% @ 50th
$Na_3V_2O_2(PO_4)_2F$	120	3.8	55% at 5C	91%@200th
$Na_2FeP_2O_7$	84	3.0	85% at 5C	~100%@80th
$Na_2MnP_2O_7$	80	3.6	NA	84% @ 15th
$Na_2NiFe(CN)_6$	65	3.2	80% at 8C	~100%@180th
$FeFe(CN)_6 \cdot 4H_2O$	120(0)	3.0	65% at 20 C	87% @ 500th
$Na_{0.61}FeFe(CN)_6$	170(54)	3.0	41% at 3.5C	~100%@150th
$Na_{1.89}Mn[Fe(CN)_6]_{0.97}$	150	3.5	81% at 20 C	75% @500th

Table 1. Comparison of Reported Cathode Materials for Sodium Ion Batteries. Reprinted with Permission from (Song et al., 2015) Copyright 2015, American Chemical Society.

*The capacity in the brackets represents the initial charge capacity by extracting the Na^+ ions. Part of reversible capacity is compensated by the Na anode in the first discharge process.

The structure of PBAs allows effective tuning of the electrochemical properties via a considerable number of degrees of freedom, including choices of various combinations of M_A and M_B transition metals together with several possible choices of interstitial ions.

Kossel's model has been widely utilized to explain the growth of the PB crystals as cubes. After a homogeneous nucleation in mother solution, solute particles or growth units, including atoms, molecules, and ions, are adsorbed on the crystal surface. The particles can migrate freely on the existing surface [usually (100) face for PBAs], and under the right conditions, they may be triggered to nucleate, eventually forming an ordered and active monolayer that has a height of one growth unit. The supersaturation condition will drive the layer-by-layer growth in a similar manner resulting in the growth of monocrystalline PB cubes. However, ideal growth only occurs in well-controlled situations. A spherical morphology is always obtained when the nucleation rate dominates the kinetics, whereas step-like morphology on the surface is usually observed under conditions in which the growth driving force is severely weakened (You et al., 2014a, 2014b; Li et al., 2015a; Wu et al., 2015a, 2016b; Huang et al., 2017). Generally, vacancies will be generated due to the excessive growth of PBA crystals when compared with the nucleation process.

Since PB is a trade name rooted in its birthplace, chemical names are more often used to differentiate numerous PBAs based on their chemical compositions. Owing to its formula $A_xM_{Ay}[M_B(CN)_6]_z$, a PBA can be called a metal hexacyanometallic compound. The first metal stands for the element in the M_AN_6 octahedra, whereas the second metal stands for the element in the M_BC_6 octahedra. Although there are a few metals capable of occupying the M_B site, Fe is the most common element in PBAs used for ion batteries. Whether a PBA is a hexacyanoferrate or a hexacyanoferric, depending on the valence of Fe^{LS} coordinated with carbon, the abbreviation is always -HCF. For example, PB can be named as FeHCF, short for iron hexacyanoferrate. Cations situated in interstitial sites can be emphasized before full name of PBAs, although they are seldom seen in an abbreviation. In addition, the color of PB can vary from blue to white or green with the insertion sodium content, and its name changes to Prussian white or Berlin green,

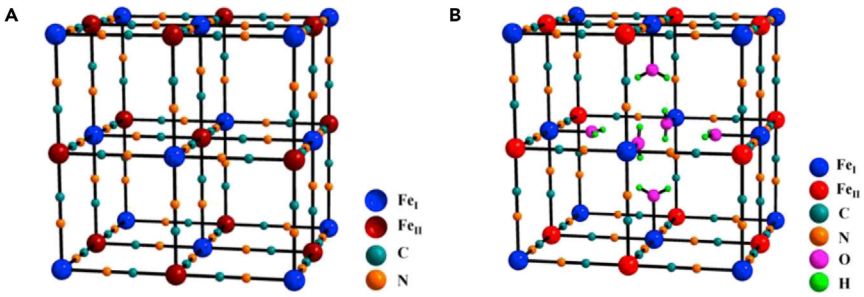

Figure 2. Schematic Diagram of Unit Cell

Unit cell of (A) perfect PB and (B) PB with coordinated water.

Fe_I stands for Fe^{3+} and Fe_{II} for Fe^{2+}. Reprinted with permission from (Wu et al., 2016a) Copyright 2016, American Chemical Society.

respectively. For other PBAs, their colors are also determined by the types of transition metals and the content of insertion cations collectively.

Energy storage in PBAs is based on the ion insertion along with the corresponding redox reaction of the transition metals in PBAs. The intercalation generally causes phase transition and color variation of PBAs. Figure 3 shows the schematic illustration of the redox mechanism and phase transition of high-quality FeHCF during sodium insertion/extraction (You et al., 2014a). Some PBAs like nickel hexacyanoferrate (NiHCF) and copper hexacyanoferrate (CuHCF) only have one redox-active site since Ni and Cu are electrochemically inert in the operating window of common electrolytes. In PBAs such as manganese hexacyanoferrate (MnHCF), FeHCF, and CoHCF, both M_A and M_B sites are redox-active centers. M_A and M_B generally have different redox potentials so that two plateaus are usually seen in their charge-discharge profiles. Table 3 shows the capacities of common PBA cathodes using different kinds of cations as charge carriers. Table 4 shows the general discharge voltage plateaus of common PBAs. However, under unique conditions the two plateaus can merge in one (Song et al., 2015; Wu et al., 2017a). Another exception is manganese hexacyanomanganate that has three plateaus because the valence of Mn^{LS} varies twice during sodium insertion/extraction (Lee et al., 2014b). The diffusion coefficient can be varied from 10^{-11}–10^{-7} cm^2 S^{-1} depending on the transition metal ions and insertion cations (Jiang et al., 2016a; Pasta et al., 2016; You et al., 2013; Ren et al., 2017; Omarova et al., 2015). For SIBs, a density functional theory (DFT) calculation was employed to determine the Na^+ diffusion in PB. The calculation results suggested that a W-shaped path bypassing through a body-center position has the lowest energy barrier for single sodium diffusion, whereas in the case of cooperative Na^+ migration, Na^+ ions preferably migrate in a step-by-step cooperative mode (You et al., 2016).

Sodium-Ion Batteries

Operating with similar chemistry, SIBs are under intense investigation to overtake LIBs in the field of large-scale energy storage taking benefit of their wide abundance, low cost, and environment friendliness (Table 5). Compared with the lithium ion that can insert/extract reversibly in various cathode materials, the larger sodium ion experiences a high resistance when diffusing through the oxide ion arrays. A variety of anode materials such as pyrolytic carbon (Komaba et al., 2011; Stevens and Dahn, 2000), alloyable metals (Qian et al., 2012; Darwiche et al., 2012; Komaba et al., 2012), and non-metal elements (Qian et al., 2013) have demonstrated remarkable anodic capacities of 300–1800 mAh g^{-1} with sufficiently high cyclability. However, cathode materials have either insufficient storage capacity or poor rate capability owing to the limited diffusion into the oxide lattices resulting from the Na^+ σ-bonding with the O-2p orbitals (Wang et al., 2013a). The relatively weaker bonding of Na ions with $C{\equiv}N^-$ groups makes PBAs appealing candidates as SIB cathodes with high, fast, and reversible ion diffusion. High-temperature synthesis is usually needed for layered oxides or polyanionic compounds, which increases the cost and difficulty for large-scale applications, whereas the mild synthesis conditions for PBAs are much more economic, environment friendly, and easy to scale up.

Theoretically, PBAs enable the insertion of two Na^+ per unit formula when both M_A and M_B feature redox activity. This leads to a potential specific capacity over 170 mAh g^{-1}, comparable with that of other kinds of cathodes, as shown in Table 6. However, such a high capacity is hardly attained because of the presence of defects, e.g., vacancies and water molecules in the open framework structure. The presence of transition

	MnHCF	FeHCF	CoHCF	NiHCF	CuHCF	ZnHCF
Cubic ($Fm\bar{3}m$)	✓	✓	✓	✓	✓	✓
Rhombohedral ($R\bar{3}$, $R\bar{3}c$)	✓	✓	✓	✓		✓
Monoclinic ($P21/n$)	✓	✓				

Table 2. Typical Crystal Structures and Space Groups of Commonly Seen PBAs [HCF: Hexacyanoferrate = $Fe(CN)_6$].

metal vacancies reduces the charge that can be stored upon the occurrence of redox reaction and the zeolitic water molecules occupy the interstitial sites that are supposed to host the diffusing sodium ion. Ideally, coordination water has to be retained to secure the stability of the crystalline structure of the open framework, whereas zeolitic water should be removed owing to its adverse effect on the initial sodium content. In general, the poor electronic conductivity also remains a key challenge for the rate capability of PBAs-based cathodes. Each system has its unique challenges to overcome for either organic or aqueous SIBs, which will be discussed in this section.

Organic Electrolyte Batteries

Batteries using organic electrolytes are supposed to enable higher energy densities relative to aqueous batteries since a much wider electrochemical window is allowed. Goodenough et al. (Lu et al., 2012) have reported about the synthesis of a series of potassium-loaded PBAs, namely, $KMFe(CN)_6$ (M = Mn, Fe, Co, Ni, Cu, Zn), and investigated their performances as cathodes in aprotic batteries. Being restricted with the non-sodium-contained ferric precursor, the performances of the obtained PBAs were limited. This work is, nevertheless, still regarded as a prelude to the development of PBAs as cathodes for aprotic SIBs for intense research in this field.

Mono-metal Hexacyanoferrate. By choosing different transitional elements, structures and properties of PBAs can be adjusted while maintaining their open frameworks. Figure 4 shows the replacement of iron by nickel and cobalt in PB structure and the consequent impact changes in their electrochemical performances. Enhanced cycle stability and increased working potential were obtained via nickel and cobalt substitution, respectively. PBAs feature, however, a capacity degradation upon cycling. Therefore, understanding the aging process is crucial for the promotion of electrochemical performance. Mono-metal hexacyanoferrates are usually used to study the Na storage mechanism and structure evolution during Na ion insertion/extraction. The most investigated hexacyanoferrates are addressed hereafter individually.

Manganese Hexacyanoferrate. Among simple PBAs, MnHCF features a high specific capacity and redox plateaus at high voltage. However, its severe crystal Jahn-Teller distortion effect affects the long-term cycling. Replacing potassium in $KMnFe(CN)_6$ by sodium greatly improved the sodium storage capacity, which reached 134 mAh g^{-1} (Wang et al., 2013a). Since this pioneer work, sodium-rich ferrate precursor $Na_4Fe(CN)_6 \cdot 10H_2O$ became the reactant of choice for the synthesis of PBAs for SIBs. The removal of interstitial H_2O, either thermally or electrochemically, from the MnHCF framework induced a structural transition (from monoclinic to rhombohedral), as shown in Figures 5A and 5B, with improved electrochemical performances (Song et al., 2015). Rhombohedral MnHCF obtained by high-vacuum thermal treatment delivered a capacity of 150 mAh g^{-1}. Another interesting phenomenon was that the plateaus associated with the redox reactions of Fe^{LS} and Mn^{HS}, at 3.17 V and 3.49 V, respectively, merge into a single flat plateau at 3.44 V as a result of the removal of the interstitial water from the lattice (Figures 5C and 5D). Yang et al. (Wu et al., 2017a) provided a comparative study of the manganese and iron redox characteristics in MnHCF electrodes with and without interstitial water using soft X-ray absorption spectroscopy (sXAS) and theoretical calculations. Distinct transition metal redox sequences were observed in the as-prepared and dehydrated $Na_xMnFe(CN)_6 \cdot zH_2O$, as shown in Figures 5E and 5F. The ligand field stabilization energy (LFSE) in transition metal compounds with well-defined spin states competes with the conventional consideration of the $Fe^{2+/3+}$ and $Mn^{2+/3+}$ redox potentials. The presence of interstitial water increases the lattice constants, which weakens the LFSE. The reversible introduction and extraction of interstitial water induced a reversible fusion and individualization of the potential plateaus.

Sottmann et al. (Sottmann et al., 2016) studied the cubic and monoclinic $Na_{1.32}Mn[Fe(CN)_6]_{0.83} \cdot zH_2O$ (z = 3.0 and 2.2) using *operando* X-ray diffraction (XRD) and X-ray absorption spectroscopy (XAS). The results evidence the Mn loss from the cathode as $NaMnCl_3$ upon cycling, which causes their aging.

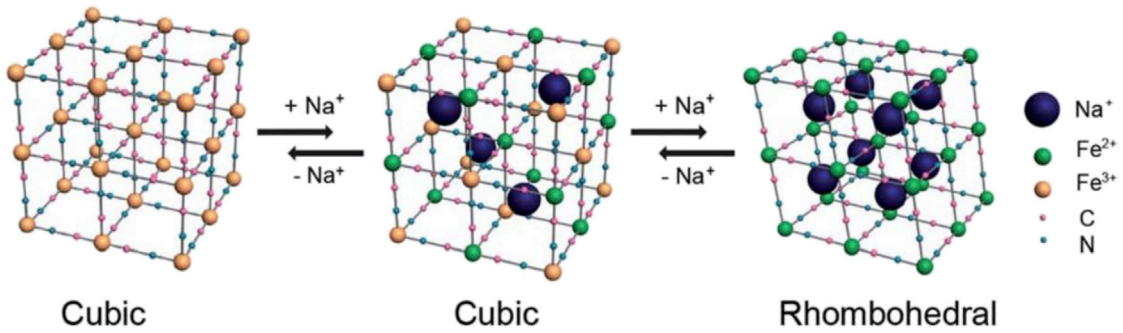

Figure 3. Schematic Illustration of the Redox Mechanism and Phase Transition of Prussian Blue
Reproduced with permission from (You et al., 2014a). Copyright 2014, The Royal Society of Chemistry.

The content of coordinated and zeolitic water in the as-prepared material emphasized the more capacity loss of the electrode. Moreover, volume changes between the sodiated and desodiated phases may also contribute to capacity degradation. Matssuda et al. (Matsuda et al., 2013) prepared a thin film electrode of MnHCF, $Na_{1.32}Mn[Fe(CN)_6]_{0.83}\cdot 3.5H_2O$, on indium tin oxides (ITO), pointing a new way for PBA growth. The electrode exhibited reversible and fast sodium ion insertion and extraction with no structural phase transition. The authors recorded a discharge capacity of 109 mAh g^{-1} and discharge voltage of 3.4 V at 0.5 C in a sodium half-cell. Jin et al. (Jo et al., 2017) reported on cubic, monoclinic, and rhombohedral MnHCF prepared in a Taylor-Couette reactor at various drying conditions/temperature. Rhombohedral MnHCF shows the highest capacity (150 mAh g^{-1}) among the three as-prepared samples.

Iron Hexacyanoferrate. FeHCF is the most widely investigated among PBA materials. Fe^{LS} and Fe^{HS} participate at different potentials in the redox reactions for sodium storage and enable a theoretical capacity of 170 mAh g^{-1}. However, the Fe^{LS} is less active, resulting in an effective lower capacity and discharge voltage. FeHCF also suffers from a poor cycling stability due to the lattice vacancies in the crystal structure and side reactions between the material and electrolyte at high voltage near 4 V. Sodium content in the as-prepared material is tightly related to the crystallinity of FeHCF.

Yang et al. (Wu et al., 2013) reported the upscalable synthesis of single-crystal FeHCF to reduce the structural imperfections. Figure 6A shows a nearly perfect cubic morphology of the FeHCF particles. The as-prepared FeHCF delivered a reversible capacity of 120 mAh g^{-1} at 0.5 C, as shown in Figure 6B, with an 87% capacity retention over 500 cycles. The investigated single crystal inherently contains the coordinated water that ensures the charge balance of the cubic $Fe^{III}Fe^{III}(CN)_6$ structure. Guo et al. (You et al., 2014a) synthesized FeHCF using $Na_4Fe(CN)_6$ as a single source precursor. In an acidic environment, $[Fe(CN)_6]^{4-}$ is slowly decomposed to Fe^{2+}, which oxidizes subsequently to Fe^{3+} due to its instability under ambient air atmosphere. Afterward, Fe^{2+}/Fe^{3+} reacts with the undecomposed $[Fe(CN)_6]^{4-}$ to form high-quality FeHCF nanocube nuclei, which grow larger with the extension of the reaction time. Cube-shaped high-quality PB (Figure 6C) with reduced number of vacancies and water content was obtained, resulting in a high specific capacity (Figure 6D) and remarkable cycling stability. Nevertheless, the sodium content was limited by the trivalent Fe formed during preparation.

The implementation of nitrogen atmosphere and vitamin C as a reducing agent allows protecting $Fe^{2+}/[Fe^{II}(CN)_6]^{4-}$ from being oxidized to $Fe^{3+}/[Fe^{III}(CN)_6]^{3-}$. The refined synthesis yields 1.63 sodium per formula, making these materials attractive from the practical point of view (You et al., 2014b). This Na-rich FeHCF with a particle size of 2–3 μm (Figure 6E) demonstrated a high capacity of 150 mAh g^{-1} (Figure 6F) and remarkable cycling performance with 90% capacity retention after 200 cycles. Air-stable $Na_{1.92}Fe[Fe(CN)_6]$ with rhombohedral structure was prepared using a hydrothermal method (Wang et al., 2015a). Figure 6G shows the inhomogeneous morphology of the as-prepared particles. The R-phase FeHCF enabled 1.92 sodium ions per formula unit, which is a record in sodium concentration among all types of PBAs. Assembling discharged cathodes with anodes containing no sodium enables manufacturing SIBs with the current LIB infrastructure. The R-FeHCF delivered a capacity of about 160 mAh g^{-1} in the first cycle (Figure 6H), reflecting the high initial Na concentration. A different approach was implemented by Dou et al. (Li et al., 2015b) to obtain Na-rich FeHCF. Introducing polyvinylpyrrolidone (PVP) and NaCl into the

PBA Cation	MnHCF	FeHCF	CoHCF	NiHCF	CuHCF
Li	190.8	190.1	188.7	94.5	92.6
Na	171.3	170.7	169.6	84.9	83.4
K	155.3	154.8	153.9	77.0	75.8

Table 3. Theoretical Capacities[a] of Common PBA Cathodes with Different Cations (Unit: mAh g^{-1})

[a]Capacities are calculated based on the sodiated sate of each material.

precursor solution provides nucleation sites and promotes sodium content, respectively. The sodium ions in the framework increase at the expense of vacancies and coordinating water in the as-prepared FeHCF, resulting in enhanced structural stability. The detailed structural evolution during sodium insertion/extraction processes was investigated *in situ* using synchrotron XRD. Rojo (Piernas-Muñoz et al., 2016) and his coworkers provided a solution to avoid the toxic NaCN production. The authors used $FeCl_2$ and $Na_4Fe(CN)_6$ as precursors to obtain sodium-rich FeHCF in inert atmosphere. In contrast to the previously described methods, the sodium content was increased by mixing the suspension after reaction with an excess of NaCl. Huang et al. (Liu et al., 2015b) found another way to increase the sodium content, which is of great importance for practical application in full batteries, via the addition of sodium citrate in the precursor. In addition, they also demonstrated that sodium cations in the large cavities of PBs have priority to occupy the 8c site, whereas in the Na-rich samples, Na^+ ions can be pushed into other 24d site through the experimental results and first-principle calculations.

Chen et al. (Liao et al., 2016) synthesized $Na_xK_yFe[Fe(CN)_6]$ and argued that K^+ influences the insertion sites of the neighboring Na^+. Chen et al. (Huang et al., 2017) reported a border-rich FeHCF synthesized by inhibitor and temperature control. The border-rich structure provides a good contact between electrode-electrolyte interfaces and increases uptake paths for Na^+ ions. With a lower energy barrier for Na^+ insertion, the as-prepared electrode exhibited a high initial capacity of 120 mAh g^{-1} and a good cycle stability. He et al. (Yan et al., 2017) demonstrated the interconnection between the electrochemical performance of FeHCF and testing conditions. FeHCF showed a good cycling stability at low temperature, whereas the capacity degraded remarkably at elevated temperature. The authors also found that the capacity fading was mainly due to side reactions on the electrode-electrolyte interface at near 4.0 V versus Na/Na^+. Balaya et al. (Rudola et al., 2017) reported on monoclinic FeHCF with a capacity of 85 mAh g^{-1} at an average discharge voltage of 3 V versus Na/Na^+.

Ye et al. (Ye et al., 2016) reported on iron-based sodium ion full batteries using FeHCF as the cathode material with an anode of FeO_x nanoparticles supported on carbon nanotubes (CNTs). The prototype had a working voltage of about 2 V, specific energy density of 136 Wh kg^{-1}, and outstanding stability at both low and high current rates.

Nickel Hexacyanoferrate. NiHCF is commonly obtained with a cubic structure. Only one pair of voltage plateaus is expected close to the equilibrium voltage of the $[Fe(CN)_6]^{4-}/[Fe(CN)_6]^{3-}$ redox couple (3.07 V versus Na/Na^+). Although Ni^{II} is electrochemically inert in NiHCF, it provides an unrivalled stability to the PB lattice. Unstrained insertion electrode materials, whose lattice parameters negligibly change (<1%) upon cycling, are of great importance for use in long-life rechargeable batteries. Therefore, structural fracture, which is the primary cause of capacity failure, is eliminated. The as-prepared NiHCF delivers a reversible capacity of 65 mAh g^{-1} and displayed a good rate performance.

Guo et al. (You et al., 2013) have investigated NiHCF in non-aqueous batteries and confirmed its zero-strain property. The negligible volume change of NiHCF not only maintained the structure stability but also preserved effective and stable transport pathways for both Na^+ and e^- among electrodes (Figures 7A–7C). This pioneering work triggered a wide research interest toward NiHCF, which later became the most widely used heteromaterial in the modification of PBAs. Dai et al. (Yue et al., 2014) synthesized mesoporous NiHCF in which extra mesoporosity was introduced into the framework of NiHCF providing large channels for facile Na^+ mass transportation in the electrode.

Stability enhancement is the focus of studies on other PBAs, whereas improving the capacity is the challenging aspect in NiHCF. Mai et al. (Ren et al., 2017) have successfully enhanced the sodium storage activity

	SIBs		KIBs		LIBs
	Aprotic (V versus Na^+/Na)	Aqueous (V versus SHE)	Aprotic (V versus Na^+/Na)	Aqueous (V versus SHE)	Aprotic (V versus Na^+/Na)
MnHCF	3.48–3.60 (Mn^{HS}) 3.26–3.40 (Fe^{LS})		~3.90 (Fe^{LS}) ~4.10 (Mn^{HS})		~3.72 (Fe^{LS}) ~3.83 (Mn^{HS})
FeHCF	3.23–3.80 (Fe^{LS}) 2.60–2.89 (Fe^{HS})	~0.90 (Fe^{LS}) ~0.15(Fe^{HS})	3.60–3.64 (Fe^{HS}) 3.91–4.10 (Fe^{LS})	~0.43 (Fe^{HS}) ~1.12 (Fe^{LS})	2.80–2.89 (Fe^{HS}) 3.70–3.80 (Fe^{LS})
CoHCF	~3.73 (Fe^{LS}) 3.04–3.12 (Co^{HS})	~1.13 (Fe^{LS}) ~0.63 (Co^{HS})			~3.39 (Co^{HS}) ~3.98 (Fe^{LS})
NiHCF	2.95–3.33 (Fe^{LS})	~0.60 (Fe^{LS})	~3.70 (Fe^{LS})	~0.70 (Fe^{LS})	~3.15 (Fe^{LS})
CuHCF	~3.32 (Fe^{LS})	~0.50 (Fe^{LS})	~3.75 (Fe^{LS})	~0.86 (Fe^{LS})	~3.10 (Fe^{LS})

Table 4. General Discharge Voltage Plateaus of Common PBAs
SHE, standard hydrogen electrode.

of NiHCF via a controllable selective etching approach. A defect-induced morphological evolution mechanism from nanocubes to nanoflower structure, as shown in Figure 7D, allowed reaching a discharge capacity of 90 mAh g^{-1}, which corresponds to the full capacity from the LS Fe redox reaction (Figure 7E).

Zhuan et al. (Ji et al., 2016) reported on a rhombohedral and cubic Na-rich NiHCF (r/c-NiHCF), which possessed a long cycle stability and an excellent rate capability, as displayed in Figure 7F. Nevertheless, NiHCF has a higher discharge voltage in the rhombohedral structure relative to the cubic counterpart, as shown in Figure 7G. First-principles calculations suggested that the high working voltage of rhombohedral phase NiHCF is correlated with the asymmetric residence of Na^+ ions in the rhombohedral framework in parallel with the low charge density at the Fe^{2+} ions. In the optimized discharged supercell of c-NiHCF (Figure 7H), Na^+ ions reside exactly at the center of the interstitial channels due to the high symmetry of the lattice, whereas for the case of r-NiHCF (Figure 7I), Na^+ ions adapt asymmetric positions at the N-coordinated sites. Thus the insertion of Na^+ leads to an enhanced electron polarization in r-NiHCF relative to c-NiHCF, resulting in charge redistribution between neighboring Ni^{2+} and Fe^{2+} ions.

Other Hexacyanoferrate Compounds. CoHCF also has two plateaus corresponding to HS Co and LS Fe. However, only few works (Wu et al., 2016b; Yuan et al., 2016) have been reported with this system due to the high cost of cobalt. Yang et al. (Wu et al., 2016b) proposed a facile citrate-assisted crystallization method to obtain low-defect CoHCF with greatly improved Na storage capacity and cycling stability. Crystallization kinetics significantly decreased in the presence of citrate ions used for the slow release of the chelating agent (Figure 8A). The reversible capacity decreased slightly from 128 to 114 mAh g^{-1} over 200 cycles, corresponding to a capacity retention of ~90%. In strong contrast, the control sample synthesized via traditional co-precipitation method shows an enormous performance degradation with only 30% of its initial capacity retained after 200 cycles. Jiao et al. (Yuan et al., 2016) fabricated CoHCF nanoparticles with a primary particle size of 30–40nm and used it as a cathode material for both LIBs and SIBs. They exhibit an outstanding rate performance exceeding 75.2% retention of initial capacity after 50 cycles at 200 mA g^{-1} when used as cathode material for SIBs. Wang et al. (Li et al., 2017a) synthesized CoHCF with a high initial sodium content (1.87 Na ions per lattice unit cell), which will be favorable for full cell fabrication.

There is little research on CuHCF used in organic system on account of the electrochemically inert Cu and its inferior stability relative to NiHCF, despite its high working potential. CuHCF prepared by Jiao et al. (Jiao et al., 2017) had a capacity of only 44 mAh g^{-1}, and the capacity retention is 57.1% after 50 cycles. The limited cycle stability may be caused by its poor crystallinity. However, considering the defects in the framework structure, this material is capable of achieving its theoretical one-electron redox capacity.

$Na_2Mn[Mn(CN)_6]$ was presented by Cui et al. (Lee et al., 2014b) as a viable positive electrode for SIBs. The manganese hexacyanomanganate (MnHCM) realized three sodium ion insertion with the oxidation process

Characteristics	Na	Li
Capacity density	1.16 Ah g^{-1}	3.86 Ah g^{-1}
Voltage versus SHE	−2.7 V	−3.0 V
Ionic radius	0.98 Å	0.69 Å
Melting point	97.7°C	180.5°C
Price (for carbonates)	0.07–0.37 € kg^{-1} [a]	4.11–4.49 € kg^{-1} [b]
Abundance	2.3%	20 ppm

Table 5. Main Characteristics of Na and Li Materials
SHE, standard hydrogen electrode.
[a]Purity:98.8%–99.2%.
[b]Battery grade:99.9%.

from $Na_3Mn^{II}[Mn^{I}(CN)_6]$ to $Na_0Mn^{III}[Mn^{III}(CN)_6]$, resulting in a high discharge capacity of 209 mAh g^{-1} at 0.2 C (theoretical capacity: 257.7 mAh g^{-1}) (Figure 8B). The authors provided chemical and structural evidence for the unprecedented storage of 50% more sodium cations than previously thought possible during electrochemical cycling. Figure 8C visualizes this ion storage mechanism. Four of the eight interstitial sites in each unit cell are occupied by two Na^+ ions on average. However, the plateau at 1.8 V, which enables one-third of the whole capacity, is too low for a cathode, which greatly affects its attractiveness.

Zhao et al. (Zhao et al., 2017a) have synthesized $Mn_3[Co(CN)_6]$ (MnHCC) nanocrystals. The as-prepared MnHCC was applied in flexible solid-state electrochemical energy devices with volumetric energy density of 4.69 mWh cm^{-3} at 10 mA cm^{-2} and a power density of 177.1 mW cm^{-3} at 20 mA cm^{-2}.

Xie et al. (Xie et al., 2016b) synthesized sodium titanium hexacyanoferrate (TiHCF), which exhibited a specific capacity over 90 mAh g^{-1} and two pairs of clear charge/discharge platforms at 3.0 V/2.6 V and 3.4 V/3.2 V, respectively. This work broadened the categories of transition metals in PBA frameworks.

Multi-metal Hexacyanoferrate. The properties of PBAs can be changed by heteroatom doping or partial substitution of the HS ions in MN_6 octahedra (M = Mn, Fe, Co, Ni), which provides an additional degree of freedom for the adjustment of the electrochemical properties. In this respect, nickel is intensively used to promote PBAs' stability owing to its electrochemical inertness. Fu et al. (Fu et al., 2017) reported that nickel doping can activate C-coordinated Fe ions (Fe^{LS}) and facilitate Na^+ diffusion within the lattice. An excellent capacity retention of 96% over 100 cycles was obtained in FeHCF with 20 at% nickel substitution in our previous work (Yu et al., 2015). Xie et al. (Xie et al., 2015) prepared a series of NiCoHCF with various nickel to cobalt ratios, and the $Na_2Ni_{0.4}Co_{0.6}Fe(CN)_6$ sample showed the best electrochemical performance, with an initial discharge capacity of 90 mAh g^{-1} and reversible capacity of 80 mAh g^{-1} after 100 cycles.

Nickel was also one of the elements used to relax the Jahn-Teller distortion in MnHCF (Yang et al., 2014; Moritomo et al., 2016). Replacing the nickel doping element by iron or cobalt induces similar effect without lowering the capacity (Moritomo et al., 2016). Jiang et al. (Jiang et al., 2016a) reported that Co doping into MnHCF stabilizes the crystal structure and also improves the electronic conductivity.

Combining Ni doping and the interstitial water reduction with sodium citrate additive yields samples with a reversible capacity of 150 mAh g^{-1} (Chen et al., 2016).

PBA Composites. Mixing PBAs with other materials is a popular strategy to boost the sodium storage. The presence of carbon during the synthesis enhances the heterogeneous nucleation of PBA and acts as electron pathway in the resulting PBA-carbon composite (Chen et al., 2016). Carbon has also been investigated as a conformal thin layer on the PBA crystals via glucose treatment (Moritomo et al., 2015). Carbon coating was replaced by perchlorate-doped polypyrrol (PPy) in the work reported by Dou et al. (Li et al., 2015c) PPy acts as a conductive coating and reduces the Mn leaching. Hu et al. (Hu et al., 2017a) also used PPy coating to enhance the electrochemical performance of MnHCF.

Types	Molecular Formula	Specific Capacity
Layered oxides	$NaCoO_2$	235.1
	$NaMnO_2$	243.6
	$NaNiO_2$	235.7
	$NaTiO_2$	260.2
	V_2O_5	236.0
Polyanion compounds	$Na_2Fe(SO_4)_3$	137.4
	Na_2FeSiO_4	276.3
	$Na_3V_2(PO_4)_3$	176.3
	$Na_3V_2(PO_4)_2F_3$	192.4
	$Na_4Fe_3(PO_4)_2(P_2O_7)$	171.8
Prussian blue	$Na_2Fe[Fe(CN)_6]$	170.7

Table 6. Theoretical Capacities[a] of Common Cathodes for Sodium Ion Batteries. (Unit: mAh g^{-1})

[a]Capacities are calculated based on the sodiated sate of each material.

Ma et al. (Yang et al., 2015) first developed a micro-cubic PB without coordinated water. Heat treatment of a graphene oxide-PB composite released the coordinated water from the PB framework via electron exchange between graphene oxide and PB (Figure 9A). The obtained reduced graphene oxide (RGO)-PB composite exhibited complete redox reactions of the Fe sites and delivered ultrahigh electrochemical performances and an excellent cycling stability (Figures 9B and 9C).

Our previous work reported an in-situ-synthesized PB@C composite as a high-performance SIB cathode (Jiang et al., 2016b) (Figure 9D). Perfectly shaped, nanosized PB cubes were grown directly on carbon chains, securing a fast charge transfer and Na-ion diffusion, as shown in Figure 9E. Superior reaction kinetics were demonstrated for the redox reactions of the Fe^{HS} couple, which rely on the partial insertion of Na ions into the PB structure to enhance electron conduction (Figure 9F).

Recently, a rapid ionic/electronic transport dynamics was observed for the PB/CNT composite, see Figures 9G–9I, even at −25°C (You et al., 2016). This work is the only one in which batteries were tested under practical conditions. It boosts the development of PBA cathode materials for SIBs, and even for all kinds of rechargeable batteries.

Prabakar et al. (Prabakar et al., 2015) reported the synthesis of highly crystalline FeHCF embedded in graphene oxide layers and the resulting superior electrochemical properties. Regulated Fe^{3+} ion release and slow crystallization with $[Fe(CN)_6]$ in the vicinity of Fe_2O_3/graphene oxide (GO) produced a high-crystallinity GO-interconnected PB (HC-PB/GO) with low $[Fe(CN)_6]$ vacancies and low content of water. When compared with synthesized PB under identical conditions without GO, the HC-PB/GO delivered a noticeably high and reversible capacity and improved cyclability as a cathode in SIBs. Luo et al. (Luo et al., 2017) fabricated a 1D tubular hierarchical structure of FeHCF nanosphere@graphene rolls by an *in situ* graphene rolls wrapping method. Zhang et al. (Nie et al., 2015) made flexible FeHCF/carbon cloth composites by a low-temperature strategy. The composites demonstrated a reversible specific capacity of 82 mAh g^{-1} at 0.2 C and long-term cycling life with 81.2% capacity retention over 1,000 cycles.

Microstructural architecture is also an efficient way to improve the performance of PB-based cathodes. Huang et al. (Wan et al., 2016) reported a green and facile synthesis of a core-shell FeHCF@NiHCF composite, which delivered a reversible capacity of 79.7 mAh g^{-1} at 200 mA g^{-1} after 800 cycles and a high coulombic efficiency of 99.3%. For the purpose of improving the conductivity of NiHCF, Nie et al. (Nie et al., 2017) built a rapid pathway for electron motion inside the open framework of NiHCF by using NiHCF powders infiltrated with the 7,7,8,8,-tetracyanoquinodimethane (TCNQ) solution. Kim et al. (Kim et al.,

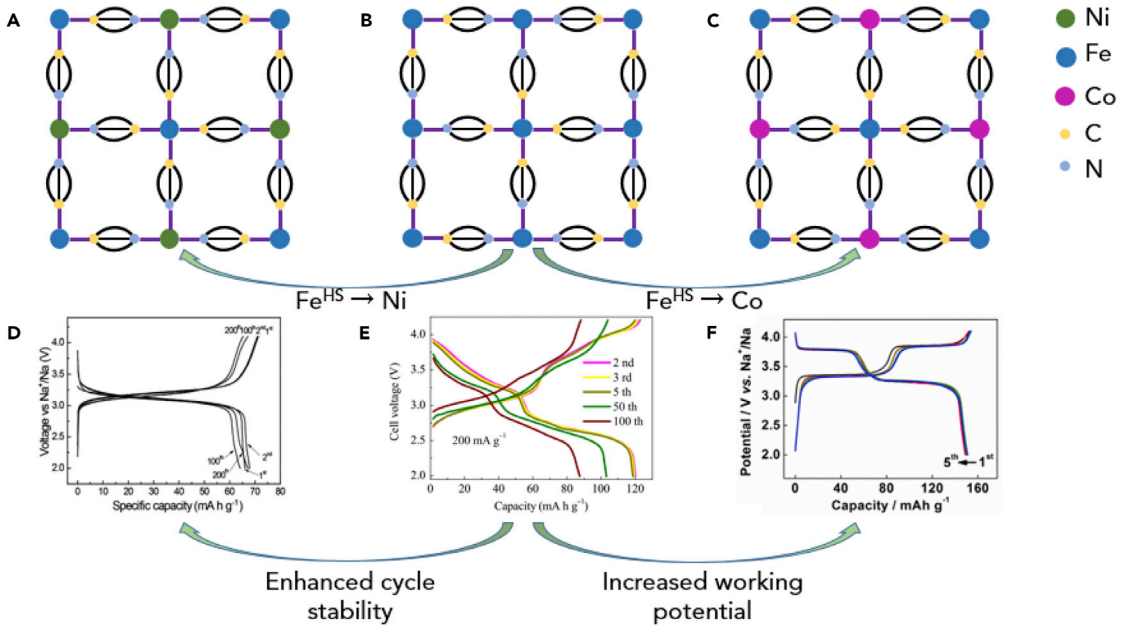

Figure 4. Electrochemical Performance Modifications of PBAs through Elemental Variation in High-Spin Sites
(A and D) NiHCF. Reproduced with permission from (You et al., 2013). Copyright 2013, The Royal Society of Chemistry.
(B and E) FeHCF. Reproduced with permission from (Liu et al., 2015b). Copyright 2015, Elsevier.
(C and F) CoHCF. Reprinted with permission from (Wu et al., 2016b). Copyright 2016, American Chemical Society.

2017) constructed dual-textured FeHCF nanocubes prepared via acid etching. Taking advantage of the porous outer layer and non-porous inner layer, dual-textured FeHCF nanocubes provided superior capacity and stability to solid FeHCF and commercially available FeHCF.

Aqueous Electrolyte Batteries

Working potentials of aqueous batteries are limited by the water decomposition voltage. Although many efforts have been made to break this limit, they are still inferior to the non-aqueous batteries (Lu et al., 2016; Zhang et al., 2015b). However, aqueous electrolyte cells are still attractive low-cost and safe alternatives for SIBs (Wessells et al., 2011a, 2011b).

Nickel Hexacyanoferrate. The stability of NiHCF also holds in aqueous systems due to its "zero-strain" property. NiHCF was reported by Cui and co-workers as a cathode for aqueous SIBs in 2011 (Wessells et al., 2011b) (Figure 10A). Sodium ion insertion/extraction was demonstrated for at least 5,000 deep cycles at high current densities, as shown in Figure 10B. The large channel diameter of the structure enables fast solid-state diffusion of Li^+, Na^+, and K^+ ions in aqueous electrolytes (Lee et al., 2014a). The authors found that the size of the alkali ion plays an important role in the electrochemical properties. By using a fast Na-ion-insertion NiHCF cathode along with an eco-friendly seawater catholyte, Senthilkumar et al. (Senthilkumar et al., 2017) have demonstrated a good cycling performance with capacity retention above 80% over 100 cycles. The average discharge voltage is as high as 3.4 V by using hybrid electrolyte and NASICON separator (Figures 10C and 10D).

Zhang et al. (Li et al., 2017c) have investigated the effect of electrolyte concentrations on the electrochemical properties of NiHCF. The authors found that high-concentration electrolyte can not only raise the working potential, owing to increased activity of Na^+ ions, but also increase the initial coulombic efficiency (99.3%) due to suppression of side reactions.

Copper Hexacyanoferrate. Considering the voltage limitation of aqueous electrolyte, making full use of the potential window is of great importance to the energy density of ion batteries. CuHCF has a discharge voltage plateau close to the decomposition voltage of water, making it an attractive cathode material in

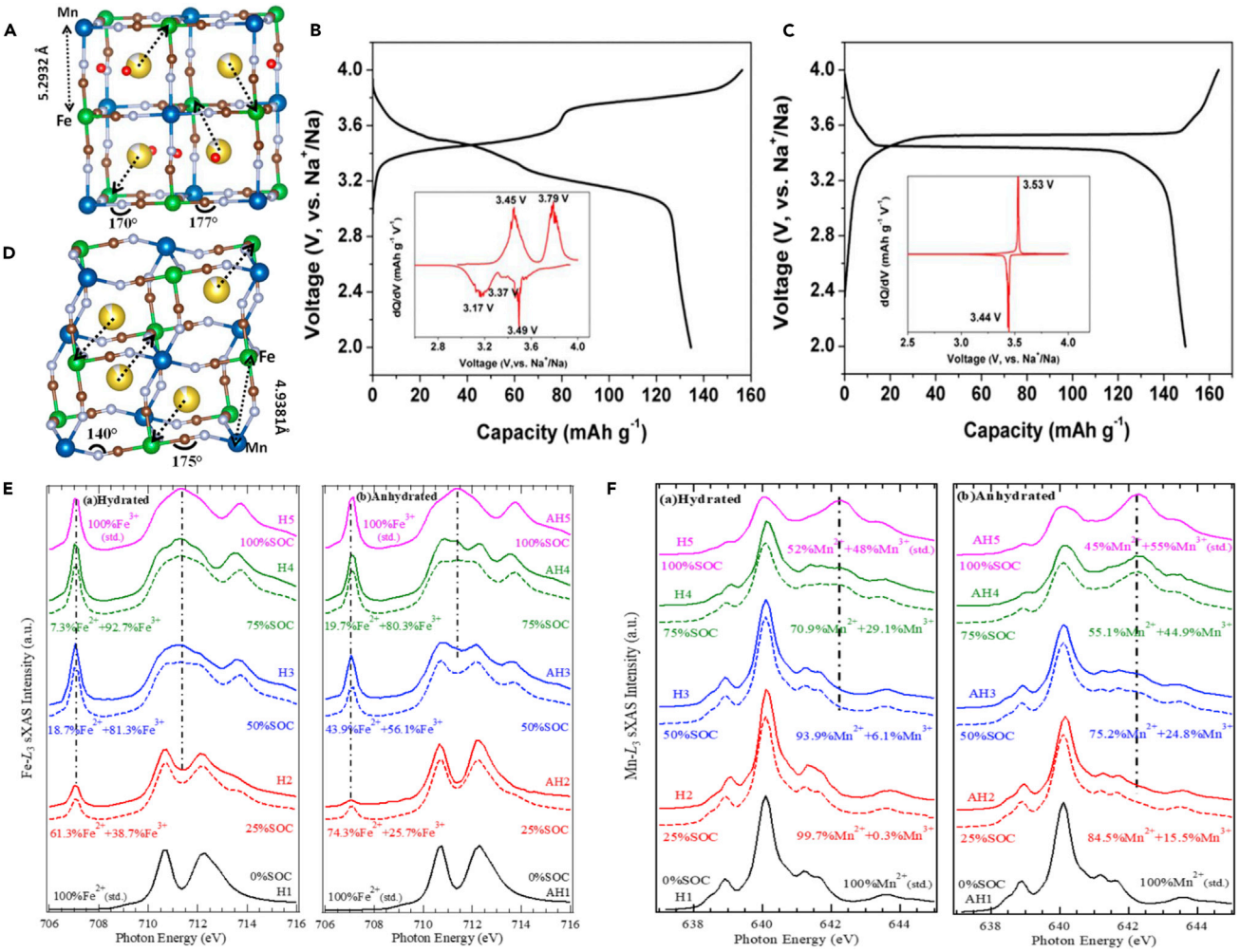

Figure 5. Structure and Electrochemical Performance of MnHCF

(A and B) Local structures of M-$Na_{2-\delta}$MnHCF (A) and R-$Na_{2-\delta}$MnHCF (B).

(C and D) Initial charge and discharge profiles of M-$Na_{2-\delta}$MnHCF (C) and R-$Na_{2-\delta}$MnHCF (D) at 0.1 C. Insets are the derivative curves. Reprinted with permission from (Song et al., 2015) Copyright 2015, American Chemical Society.

(E and F) Fe L_3-edge (E) and Mn L_3-edge (F) sXAS spectra collected on a series of electrode samples cycled to different states of charge (SOCs): M-$Na_{2-\delta}$MnHCF (left); R-$Na_{2-\delta}$MnHCF (right). Reprinted with permission from (Wu et al., 2017a) Copyright 2017, American Chemical Society.

aqueous batteries. Jia et al. (Jia et al., 2014) found that sodium ion insertion and extraction behaviors were controlled by the solid-phase diffusion process in the CuHCF electrode. Cui et al. (Wessells et al., 2012) investigated CuHCF as a cathode material for aqueous SIBs along with NiHCF and a series of their composites. The authors demonstrated that the reaction potential of CuNiHCF nanoparticles may be tuned by controlling the ratio of copper to nickel in these materials. With the decline of nickel content in CuNiHCF, the stability increased at the expense of the working voltage, as shown in Figure 10E. A full aqueous battery with CuHCF cathode and MnHCM anode was reported with a high-rate, 96.7%/84.2% round-trip energy efficiency at 5 C/50 C, respectively (Pasta et al., 2014). No measurable capacity loss was noticed even after 1,000 deep-discharge cycles (Figure 10F).

Jiang et al. (Jiang et al., 2017a) built a full battery using a CuHCF cathode and a $NaTi_2(PO_4)_3$ anode possessing both high power density (3006 W kg^{-1}) and high energy density (56 W hr kg^{-1}) as shown in Figure 10G. The authors also found that the most stable interstitial site changes from the face-centered site (24d) to the body-centered site (8c) for large diffusing ions. The insertion voltage for the alkali cations also increases with the ionic size.

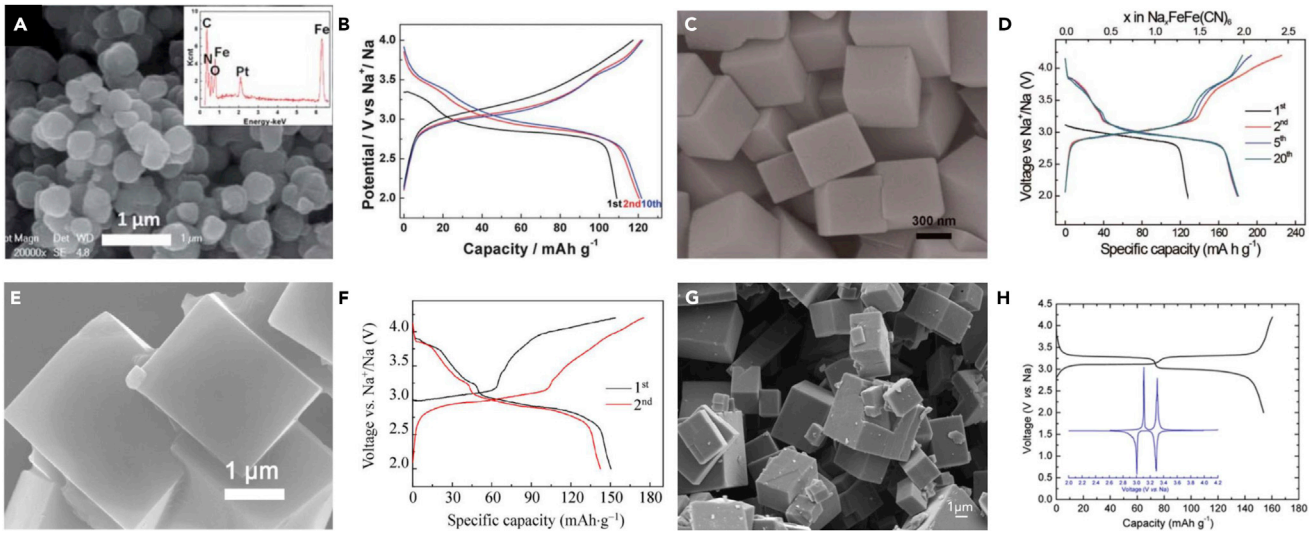

Figure 6. Scanning Electron Microscopic Images and Galvanostatic Charge-Discharge (GCD) Profiles of FeHCF

(A and B) (A) Scanning electron microscopic image and (B) GCD profiles of $FeFe(CN)_6$; inset shows energy dispersive X-ray spectroscopy (EDX) elemental analysis results. Reproduced with permission from (Wu et al., 2013). Copyright 2013, The Royal Society of Chemistry.

(C and D) (C) Scanning electron microscopic image and (D) GCD profiles of FeHCF prepared by single iron source method. Reproduced with permission from (You et al., 2014a). Copyright 2014, The Royal Society of Chemistry.

(E and F) (E) Scanning electron microscopic image and (F) GCD profiles of sodium-rich FeHCF. Reproduced with permission from (You et al., 2014b). Copyright 2015, Springer Nature.

(G and H) (G) Scanning electron microscopic image and (H) GCD profiles of R-FeHCF; inset shows chronoamperograms. Reprinted with permission from (Wang et al., 2015a) Copyright 2015, American Chemical Society.

Other Hexacyanoferrate Compounds. VHCF, MnHCF, FeHCF, and CoHCF were introduced as cathodes to the aqueous system as well and the delivered capacities were comparable with those of non-aqueous batteries (Wu et al., 2015a, 2015b; Fernández-Ropero et al., 2016; Nakamoto et al., 2017; Lee et al., 2017; Paulitsch et al., 2017). Nevertheless, their inappropriate voltage plateaus make them less attractive.

VHCF provides the improved capacity of 91 mAh g^{-1} under a current density of 110 mA g^{-1} in aqueous electrolyte (Lee et al., 2017). Paulitsch et al. (Paulitsch et al., 2017) reported $Na_2VO_x[Fe(CN)_6]$ thin film with a very positive half-charge potential in acidic media with a specific capacity of ~80 mAh g^{-1} (Figure 10H). The well-known leaching effects related to the nature of the alkali metal cations during insertion and extraction were surprisingly reduced in the case of VHCFs.

Low-defect FeHCF nanocube crystals exhibit a capacity of 125 mAh g^{-1} and a remarkably long cycle life with 83% capacity retention over 500 cycles (Wu et al., 2015a). This performance considerably exceeds that of the aqueous Na-storage cathodes reported so far and is capable of serving as a high-performance cathode for aqueous SIBs. Similarly, Rojo et al. (Fernández-Ropero et al., 2016) reported a remarkable cycling stability and near-100% coulombic efficiency for $Na_{1-x}Fe_{1+(x/3)}[Fe(CN)_6]_y \cdot yH_2O$ in aqueous electrolyte. Hereby, the authors suppressed the process at high voltage. FeHCF was also used as bipolar material, which works as both the cathode and anode materials in a battery (Zhang et al., 2017b). The as-obtained full aqueous battery exhibited a capacity of 32 mAh g^{-1} at 20 C. Wang et al. (Cai et al., 2017) compared the electrochemical performance of FeHCF with high and low qualities as cathodes for aqueous SIBs, confirming the importance of crystallinity for the electrochemical performance of FeHCF in aqueous and non-aqueous batteries.

Yang et al. (Wu et al., 2015b) also used vacancy-free CoHCF nanocubes synthesized by a controlled crystallization reaction in an aqueous SIB. Owing to its perfect lattice framework with two redox-active sites, this material exhibited a high reversible capacity of 130 mAh g^{-1}, a strong rate capability at 20 C, and superior cyclability with 90% capacity retention over 800 cycles.

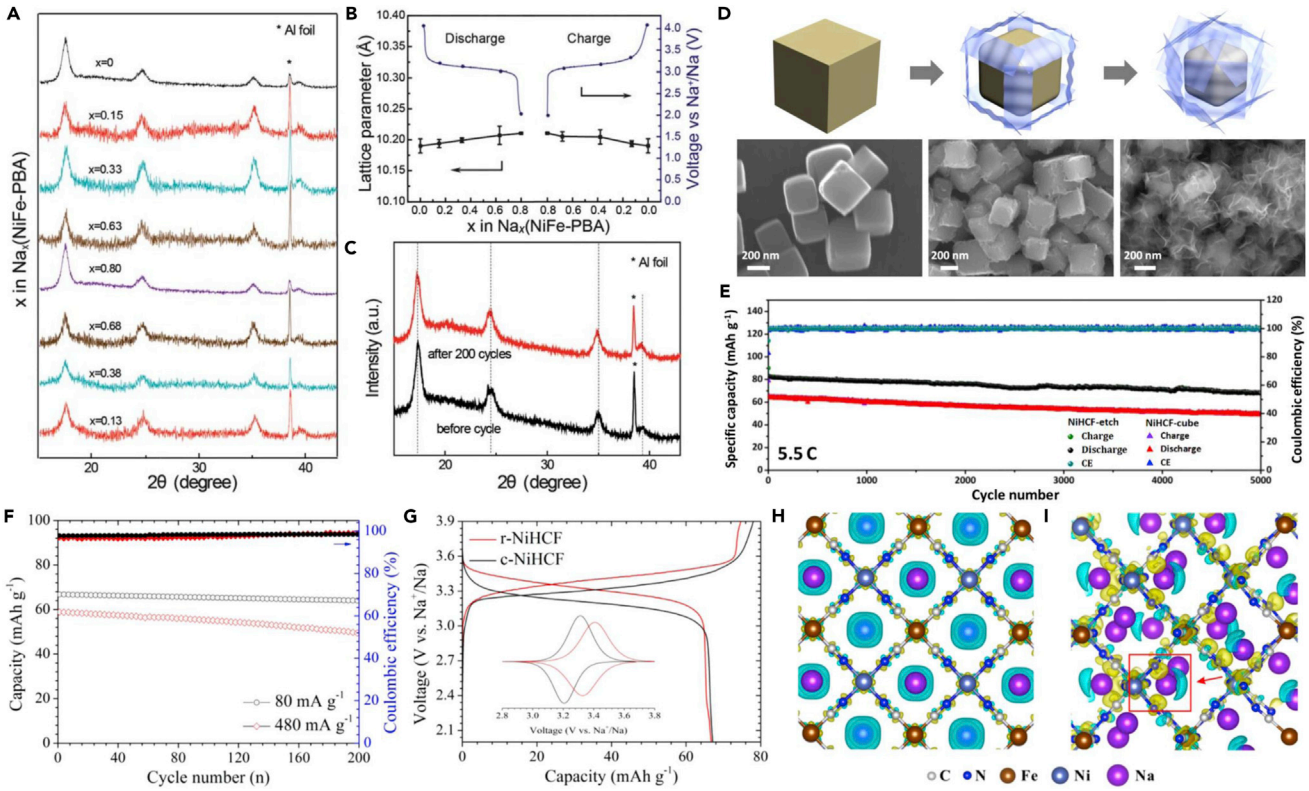

Figure 7. Structure, Morphology, and Electrochemical Performance of NiHCF

(A) *Ex situ* XRD patterns of NiHCF cathodes at various charge/discharge states.

(B) Lattice parameter variation as a function of x in Na_x(NiHCF).

(C) XRD patterns of NiHCF cathodes before and after 200 cycles. Reproduced with permission from (You et al., 2013). Copyright 2013, The Royal Society of Chemistry.

(D) Schematic diagrams and scanning electron microscopic images of the NiHCF products after an etching time of 0 hr (left), 0.5 hr (middle), and 6 hr (right).

(E) Cycling stability of NiHCF-cube and NiHCF-etch. Reprinted with permission from (Ren et al., 2017) Copyright 2017, American Chemical Society.

(F) Cycle performance of r-NiHCF.

(G) Galvanostatic charge-discharge profiles of r-NiHCF and c-NiHCF, inset shows chronoamperograms.

(H and I) Differential charge density analysis of c-NiHCF (H) and r-NiHCF (I). Reprinted with permission from (Ji et al., 2016) Copyright 2016, American Chemical Society.

Manganese-doped CoHCF with different Mn/Co ratios was revealed to combine the properties of both MnHCF and CoHCF (Pasta et al., 2016). The authors demonstrated that C-coordinated Fe preserves the crystal structure and enables an outstanding kinetics, whereas the N-coordinated Co and Mn ions have a slower kinetic regime due to structural distortions resulting from the weak N-coordinated crystal field.

Li et al. (Li et al., 2017b) reported the effect of Co substitution on charge/discharge performance of NiCoHCF. It is revealed that the material undergoes a reversible three-step single-phase reaction mechanism during Na extraction through sequential electrochemical oxidation of nitrogen-coordinated Co^{2+} ions, carbon-coordinated Fe^{2+} ions with nickel-rich MN_6 (M = Ni, Co) neighbors, and carbon-surrounded Fe^{2+} ions with cobalt-rich MN_6 environment.

Miguel et al. (Oliver-Tolentino et al., 2016) studied ZnHCF, $Zn_3Na_2[Fe(CN)_6]$, which has a rhombohedral structure totally different from all the other types of PBAs. It is stable in acidic and neutral aqueous solutions and appears to be an attractive material for sodium ion-based batteries.

Potassium Ion Batteries

Two nearest-neighbor alkali metals (K and Mg) have drawn much attention during the past two decades. K is indeed a competitive option even relative to Li. A key benefit of potassium batteries is the exceptionally

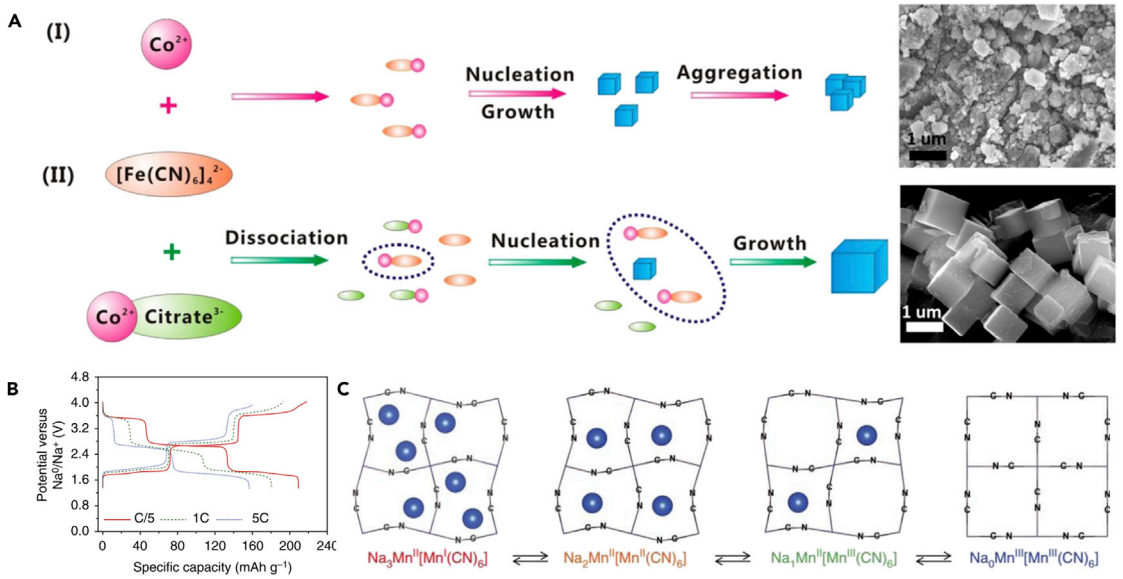

Figure 8. Growth of CoHCF and Sodium Storage Mechanism of MnHCM

(A) Schematic illustration of the conventional co-precipitation method (I) and the citrate-assisted controlled crystallization process (II) for the synthesis of $Na_2CoFe(CN)_6$. Reprinted with permission from (Wu et al., 2016b) Copyright 2016, American Chemical Society.

(B) Galvanostatic charge-discharge profiles of MnHCM at C/5.

(C) Schematic diagrams of the changes in structure of MnHCM during battery cycling. Reproduced with permission from (Lee et al., 2014b). Copyright 2014, Springer Nature.

negative potential of the K/K^+ redox couple (−2.936 V versus standard hydrogen electrode) (Eftekhari et al., 2017). This low voltage range means high energy density when used in a full cell. Another advantage of KIBs is the availability of highly promising anode and cathode materials for the insertion of K^+ ions. For example, graphite, which is unable to intercalate sodium ions, allows reversible potassium insertion and extraction. Most KIBs are aqueous systems because of the good solubility of potassium.

Aqueous Potassium Ion Batteries

As early as 2004, Eftekhari (Eftekhari, 2004) has reported PB as a cathode for potassium secondary batteries and gave a further suggestion on its application as a cathode material for LIB as well, but his work was not brought into focus. PBAs for rechargeable batteries returned to the spotlight when Cui and his co-workers demonstrated the insertion/extraction of sodium and potassium ions in NiHCF (Wessells et al., 2011b).

For instance, CuHCF nanoparticles could be operated as a cathode material in an aqueous electrolyte of 1 M KNO_3 (Wessells et al., 2011a). A full battery consisting a CuHCF cathode and an activated carbon/polypyrrole hybrid as anode featured a high-rate, 95%/79% round-trip energy efficiency at 5 C/50 C, respectively (Pasta et al., 2012). The battery had no capacity loss after 1,000 deep-discharge cycles.

Wang et al. (Su et al., 2017b) reported the synthesis of high-potassium-content FeHCF-dehydrated nanocubes and their performances as electrodes in aqueous electrolyte KIBs. The potassium-rich FeHCF can supply two electrons per formula unit and therefore delivered exceptionally high capacities in aqueous KIBs (up to 120 mAh g^{-1}). Zarbin et al. (Nossol et al., 2016) have grown FeHCF on iron-decorated single-walled CNT (SWCNT) and iron-filled multi-walled CNT (MWCNT) to obtain flexible CNT/PB nanocomposite thin films. SWCNT/PB showed a more reversible character than MWCNT/PB, while the MWCNT/PB film presented a high stability upon the application of several voltammetric cycles.

Ghasem et al. (Ghasemi et al., 2015) have grown NiFeHCF together with graphene oxide, which electrochemically reduced to graphene on stainless steel via electrophoretic deposition. The as-prepared electrode had a capacity (67.77 mAh g^{-1}) that is superior to both constituents.

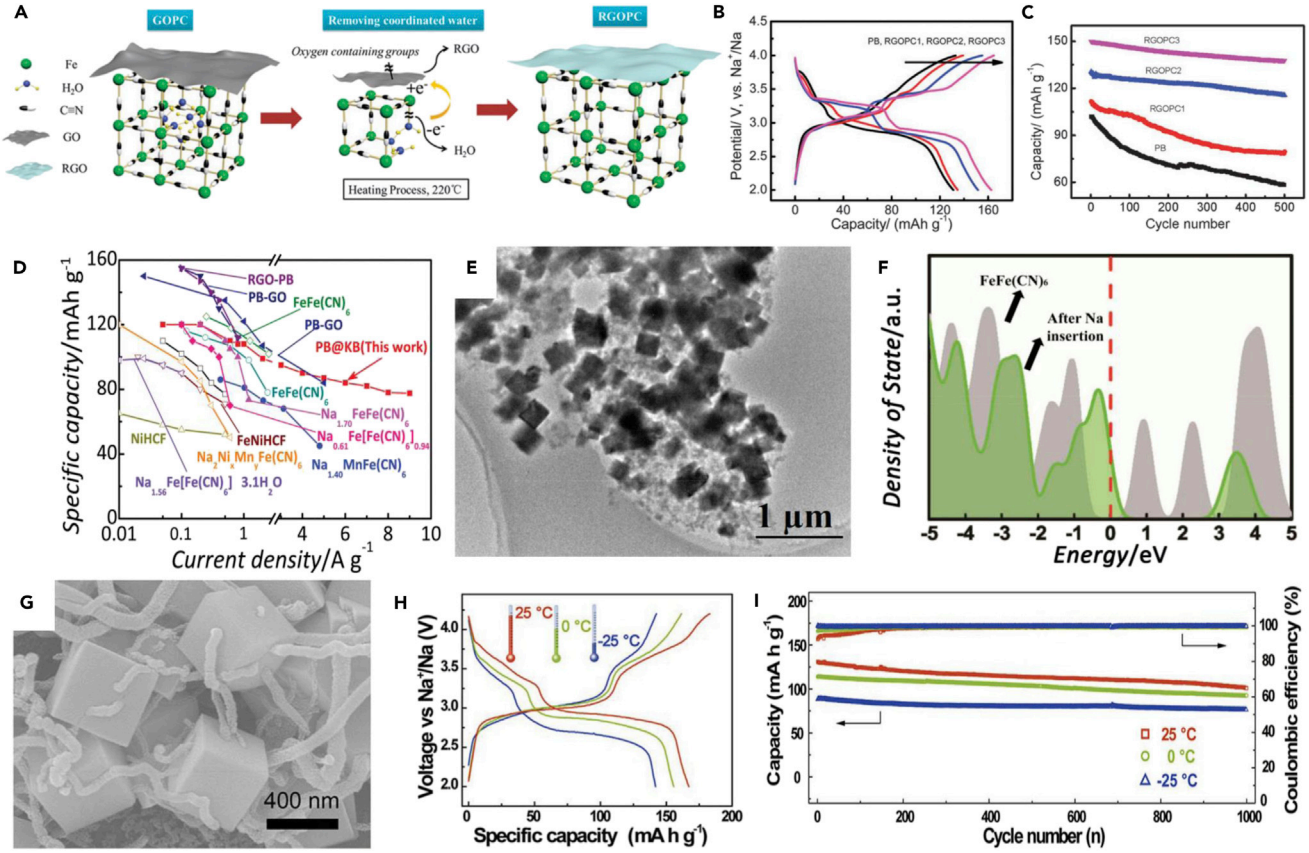

Figure 9. Morphology and Electrochemical Performance of PB Composites

(A) Schematic mechanism for the removal of coordinated water from reduced graphene oxide (RGO)/PB composite (RGOPC).

(B) The second galvanostatic charge-discharge (GCD) profiles of PB, RGOPC1, RGOPC2, and RGOPC3 at 30 mA g^{-1}.

(C) Cycling performances of PB, RGOPC1, RGOPC2, and RGOPC3 at 200 mA g^{-1}. Reproduced with permission from (Yang et al., 2015). Copyright 2015, The Royal Society of Chemistry.

(D) Rate performance of PB@C electrode compared with that of previously reported Prussian blue cathodes.

(E) Typical scanning transmission electron microscopic image of PB@C.

(F) Density of states (DOS) spectrum of PB before (gray) and after (green) insertion of Na. The Fermi level (red dashed line) was set to zero. Reproduced with permission from (Jiang et al., 2016b). Copyright 2016, Wiley-VCH.

(G) Scanning electron microscopic image of the PB/CNT.

(H) GCD profiles at 0.1 C of the PB/CNT cathode at different temperatures.

(I) Cycling performance at 2.4 C of the PB/CNT cathode at different temperatures. Reproduced with permission from (You et al., 2016). Copyright 2016, Wiley-VCH.

The influence of the precursors, namely, potassium ferrocyanide and potassium ferricyanide, on the particles sizes of PB and Prussian green (PG) under identical reaction conditions have been investigated by Padigi et al (Padigi et al., 2015b). The authors interpreted the increased capacity of PG relative to PB batteries to be a result of the smaller particle size of PG, which resulted in greater accessibility of the cathode to K^+ ions.

Non-aqueous Potassium Ion Batteries

Lei et al. (Zhang et al., 2017a) reported FeHCF, which exhibited a high discharge voltage of 3.1–3.4 V, a high reversible capacity of 73.2 mAh g^{-1}, and great cyclability at both low and high rates with a very small capacity decay of about 0.09% of the cathode during cycling. Chong et al. (Chong et al., 2017) reported FeHCF nanoparticles for non-aqueous KIBs with a high discharge capacity of 118.7 mAh g^{-1} at an operating voltage of 3.34 V. Nazar et al. (He and Nazar, 2017) reported a very strong effect of crystal size on electrochemical behavior. FeHCF with size of 20 nm was found to deliver a close-to-theoretical reversible capacity of 140 mAh g^{-1} with two well-defined plateaus at 4.0 V and 3.2 V versus K/K^+ upon discharge.

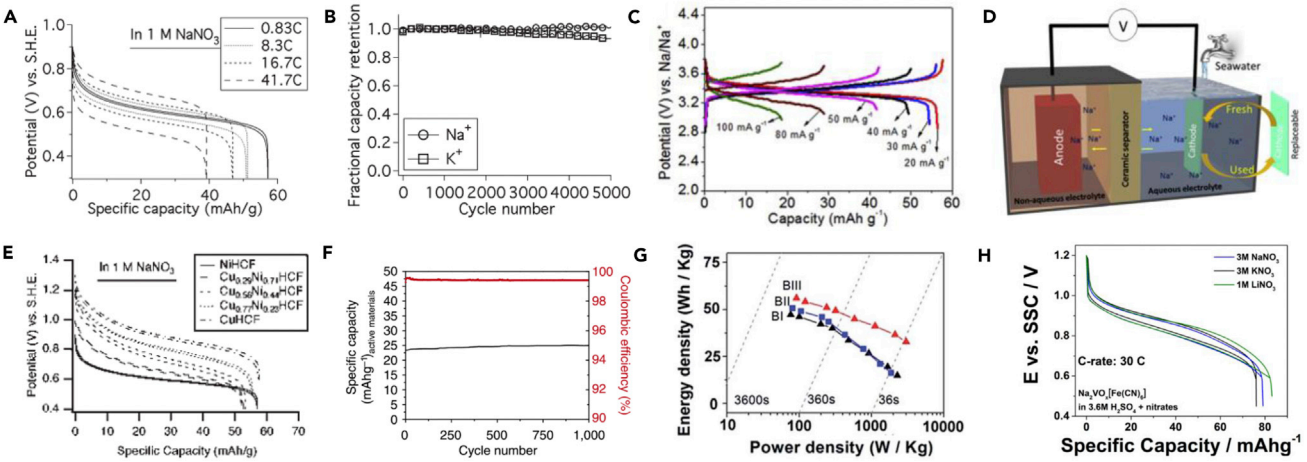

Figure 10. Electrochemical Performance of PB in Aqueous Sodium Ion Batteries

(A) Galvanostatic charge-discharge (GCD) profiles of NiHCF at various rates.

(B) Cycle performance of NiHCF in 1M $NaNO_3$ and KNO_3 solution at an 8.3 C rate. Reprinted with permission from (Wessells et al., 2011b) Copyright 2011, American Chemical Society.

(C) GCD profiles of NiHCF in a duel electrolyte battery at different current densities.

(D) Schematics of the proposed sodium ion hybrid electrolyte battery system with a replaceable cathode. Reproduced with permission from (Senthilkumar et al., 2017). Copyright 2017, Elsevier.

(E) GCD profiles of CuNiHCF in 1 M $NaNO_3$. Reprinted with permission from (Wessells et al., 2012) Copyright 2012, American Chemical Society.

(F) Cycle performance of the CuHCF-MnHCM cell at a rate of 10 C. Reproduced with permission from (Pasta et al., 2014). Copyright 2011, Springer Nature.

(G) Ragone plot of BI: CuHCF/Li^+ + Na^+/TiP_2O_7; BII: CuHCF/Li^+ + K^+/TiP_2O_7; BIII: CuHCF/Na^+ + K^+/TiP_2O_7. Reproduced with permission from (Jiang et al., 2017a). Copyright 2017, The Royal Society of Chemistry.

(H) GCD profiles at 30 C rate for the $Na_2VO_x[Fe(CN)_6]$ films in 1 M $LiNO_3$, 3 M $NaNO_3$, and 3 M KNO_3 with 3.6 M H_2SO_4 electrolytes. Reprinted with permission from (Paulitsch et al., 2017) Copyright 2017, American Chemical Society.

Jiang et al. (Jiang et al., 2017b) reported MnHCF as a cathode material for aprotic KIBs. MnHCF enables 115 mAh g^{-1} discharge capacity with two voltage plateaus at 3.9 and 4.1 V versus K/K^+. Komaba et al. (Bie et al., 2017) employed MnHCF and FeHCF as cathode materials for non-aqueous KIBs. MnHCF delivered a high capacity of 141 mAh g^{-1} at 3.8 V, resulting in a comparable energy density to that of $LiCoO_2$ in K half-cell. The authors also found structure change from monoclinic to tetragonal via cubic phase during K^+ extraction. Wu et al. (Wu et al., 2017b) also reported on MHCF (M = Fe, Co, Ni or Cu) as cathodes for non-aqueous KIBs. Among these materials, FeHCF exhibits the highest reversible capacity of 110 mAh g^{-1} with high potential above 3.2 V versus K/K^+.

Lithium Ion Batteries

The small size of lithium ions relative to sodium and potassium makes its diffusion in the open framework more favorable. The application of PBAs for LIBs sets a good example for non-lithium batteries' research back-feeding LIBs. In contrast to KIBs, LIBs are always non-aqueous systems because of the lack of suitable lithium salt in aqueous systems. Okubo et al. (Okubo and Honma, 2013) synthesized $Mn_{0.5}Cu_{0.5}$HCF nanoparticles as cathode materials for LIBs. Heterometal substitution suppressed phase separation induced by over-lithiation, leading to both a long cycle life and a high rate capacity. Chen et al. (Shen et al., 2014) have shown that nanosized FeHCF (95 $mAhg^{-1}$) features superior cycling and rate performances relative to micrometer-sized FeHCF cubes (138 $mAhg^{-1}$). Yang et al. (Wu et al., 2016a) reported FeHCF nanocrystals with well-controlled lattice defects and perfect nanocubic morphology, which exhibit a high Li storage capacity (160 mAh g^{-1}), a strong rate performance at 24 C, and a superior cycle stability with 90% capacity retention over 300 cycles.

Marzhana et al. (Omarova et al., 2015) reported NiHCF as a cathode in LIBs with a working potential of 3.3 V (versus Li/Li^+) and stable cycling performance within a wide range of current densities.

Asakura et al. (Asakura et al., 2013) designed core@shell particle heterostructures as the cathode material for Li ion storage. Composed of a high-capacity $K_{0.1}Cu[Fe(CN)_6]_{0.7}\cdot 3.8H_2O$(CuHCF) core and

lower capacity but highly stable shell of $K_{0.1}Ni[Fe(CN)_6]_{0.7}\cdot 4.1H_2O$, the heterostructure reconciliates high capacity and long cycle stability. $V_{1.07}Cu_{0.35}$-HCF was prepared by Xie et al. (Xie et al., 2016a), and its annealed derivatives were investigated for their electrochemical behavior as lithium cathode materials. The insertion of Li ions was improved upon the removal of zeolitic water from the framework.

Carbon materials and conductive polymers were also mixed with PBAs for LIBs (Wong et al., 2015; Wang et al., 2013b). Wong et al. (Wong et al., 2015) reported an efficient and adaptable method for the synthesis of lithium hexacyanoferrate/conductive polymer composites for LIB cathodes. Composites consisting of $LiFe^{III}Fe^{II}(CN)_6$, PPy, and poly(sodium 4-styrenesulfonate) (PSS) enable a capacity of about 120 mAh g^{-1} at a current of 20 mA g^{-1}. Nesper et al. (Wang et al., 2013b) prepared MnHCF/graphene composite by ball milling of graphene oxide and nanoparticles of MnHCF. The composite exhibited an enhanced electrochemical performance compared with pure MnHCF with a specific capacity of 150 mAh g^{-1} at an average of 3.8 V versus Li/Li^+ and a good cyclability.

Rojo et al. (Piernas-Muñoz et al., 2014) used $K_{0.88}Fe_{1.04}[Fe(CN)_6]\cdot yH_2O$ as an anode in LIBs and reported a capacity of 450 mAh g^{-1} at 8.75 mA g^{-1} in the low-voltage window from 0.005 to 1.6 V (versus Li^+/Li). Xiong et al. (Xiong et al., 2015) also used MnHCF as an anode for LIBs and reported a reversible capacity of 295.7 mAh g^{-1} after 100 cycles at 200 mA g^{-1}. Chen et al. (Sun et al., 2016) used $Ti_{0.75}Fe_{0.25}[Fe(CN)_6]_{0.96}\cdot 1.9H_2O$ as an anode for LIBs and SIBs. The TiFe-HCF reacted with lithium following a conversion reaction mechanism. It enables a high reversible capacity of 350 mAh g^{-1} versus Li^+/Li, much more than that of sodium (100 mAh g^{-1}).

Zhang et al. (Nie et al., 2014) reported nanoparticles of cobalt hexacyanocobaltate (CoHCC) and manganese hexacyanocobaltate (MnHCC) with the chemical formula $M_3^{II}[Co^{III}(CN_6)]_2\cdot nH_2O$ operated as anodes for LIBs. The $Co_3[Co(CN)_6]_2$ material exhibits electrochemical activity in the voltage range of 0.01–3 V versus Li/Li^+ with a reversible capacity of 299.1 mAh g^{-1}.

Polyaniline (PANI) was uniformly coated on the surface of PBA nanocubes by Cao and co-workers (Zhang et al., 2017c). The obtained core-shell PBAs@PANI nanocubes enable excellent lithium storage with a reversible capacity of 626 mAh g^{-1} compared with the uncoated PBAs (203 mAh g^{-1}) after 500 cycles at a current density of 1 A g^{-1}.

Multivalence Ion Batteries

Multivalent ions have been of interest for rechargeable batteries for many years because a doubly or triply charged ion can accept two/three electrons for a single ion. For intercalation-type batteries, this means fewer ions would need to diffuse into a lattice for a given capacity, which could result in less severe lattice distortion and more stable cells (Kuperman et al., 2017). New energy storage chemistries based on multivalent ions can theoretically improve the energy density and reduce the cost of batteries. However, lack of suitable cathode materials with desirable capacity and long-term stability severely restricts the application of multivalent ion batteries (Hu et al., 2017b, 2018). A key issue with multivalent ion insertion is the ion mobility in host materials, which is highly dependent on the size and charge of the guest ion. Large and multivalent ions could easily fall into a combined energetic/steric trap and block the ion mobility. Therefore the choice of host materials is limited to a great extent. Fortunately, requirements of multivalent ion batteries can be satisfied by PBAs possessing rigid open framework. One type of PBA may allow insertion of several kinds of ions. For instance, Lipson et al. (Lipson et al., 2016) demonstrated the ability of NiHCF to electrochemically insert Mg, Ca, and Zn ions from a non-aqueous electrolyte. CuHCF presented by Cui et al. (Wang et al., 2015b) allowed for the reversible insertion of monovalent, divalent, and trivalent ions from aqueous solutions beyond what was achieved in previous studies.

Zinc Ion Batteries

Zinc ion multivalence batteries are the most widely studied. Lu et al. (Lu et al., 2016) fabricated aqueous Na-Zn hybrid batteries assembled based on NiHCF and Zn electrodes. The rational combination of two materials with a neutral aqueous electrolyte allows the operation of the battery at a voltage close to 1.5 V, and the cell delivers a specific capacity of 76.2 mAh g^{-1} and 81% capacity retention after 1,000 cycles.

Jia et al. (Jia et al., 2015b) reported on an aqueous zinc battery based on a CuHCF cathode and a zinc anode. A specific discharging capacity of 56 mAh g^{-1} was obtained at 20 mA g^{-1}. Mantia et al. (Trocoli and La Mantia, 2015) also reported a zinc ion battery based on CuHCF and zinc foil in a 20 mM solution

of zinc sulfate. The voltage of this battery was as high as 1.73 V. The system shows cyclability, rate capability, and specific energy values near those of lithium ion organic batteries composed of $Li_4Ti_5O_{12}$ and $LiFePO_4$ at a rate of 10 C. The effects of Zn^{2+} insertion and H_2 evolution on the performance of the battery were discussed in detail. Kasiri et al. (Kasiri et al., 2016) revealed that the nature of the cation plays a role in the stability of the active material, as well as the concentration of zinc ions in the solution. The authors observed a capacity fading and attributed it to the phase transition of CuHCF rather than to the active material dissolution.

A unique zinc ion battery based on a ZnHCF cathode and a zinc anode was prepared by Zhang and co-workers (Zhang et al., 2015b). Owing to its high working voltage of 1.7 V, a specific energy density of 100 Wh kg^{-1} was calculated based on the total mass of active electrode materials. The authors have developed a simple co-precipitation method to tune the particle morphology of ZnHCF by adjusting the processing parameters at room temperature (Zhang et al., 2015a). Cuboctahedron morphology ZnHCF was chosen as the cathode, whereas zinc was used as the anode to manufacture the aqueous zinc ion battery in 3 M $ZnSO_4$ electrolytes. The battery delivered an energy density of 104 Wh kg^{-1} with an average operating voltage of 1.73 V. Gupta et al. (Gupta et al., 2016) demonstrated that the loss in capacity was a combined effect of Zn^{2+} ion poisoning at the PBA cathode and the formation of dendrite in the zinc anode. The authors addressed both issues via the use of a dual ion (Na^+ as the primary charge carrier) electrolyte and hyper-dendritic zinc (HD Zn) as the anode.

Endres et al. (Liu et al., 2016) used FeHCF as the cathode material in a zinc battery with a bio-ionic liquid-water mixture as electrolyte. The cell exhibited a well-defined discharge voltage plateau of ~1.1 V with a specific capacity of about 120 mAh g^{-1} at 0.1 C. Chae et al. (Chae et al., 2017a) have shown that NiHCF can also be used as a cathode in an organic-electrolyte-based rechargeable zinc ion battery. This cell showed a reversible discharge capacity of 55.6 mAh g^{-1} at 0.2 C rate with the discharge voltage at 1.19 V (versus Zn/Zn^{2+}).

Magnesium Ion Batteries

Mg^{2+} insertion/extraction in CuHCF was reported using aqueous electrolytes (Mizuno et al., 2013). Owing to fast transport of hydrated Mg^{2+}, excellent rate capability was achieved. The capacity was about 50mAh g^{-1} at a current density of 0.1 A g^{-1}. Kim et al. (Kim et al., 2016) found that FeHCF allows a reversible inward and outward diffusion of Mg^{2+} in the presence of Na^+ ions. Yagi et al. (Yagi et al., 2015) reported CuHCF as a cathode for both aqueous and aprotic Mg batteries. The authors measured the redox potential of CuHCF at approximately 3 V versus Mg/Mg^{2+} in both aqueous and organic electrolytes.

Hong et al. (Chae et al., 2017b) reported Mg^{2+} storage of NiHCF in organic electrolyte with a discharge capacity of 48.3 mAh g^{-1} at 0.2 C and an average discharge voltage of 2.99 V (versus Mg/Mg^{2+}). The authors found that the magnesium ions in NiHCF are positioned at the center of the large interstitial cavities. Xia et al. (Chen et al., 2017b) established an aqueous Mg-metal battery consisting of a NiHCF cathode, a polyamide anode, and a Mg^{2+} aqueous electrolyte. The cell exhibits a maximum cell voltage of 1.5 V and a supercapacitor-like high power, and it can be cycled 5,000 times.

Calcium Ion Batteries

Lipison et al. (Lipson et al., 2015) reported a capacity of 80 mAh g^{-1} with Ca ion battery utilizing MnHCF as cathode. The investigated PBA enabled a reversible Ca ion insertion in an anhydrous electrolyte. Based on XAS analysis, the authors confirmed that only manganese changes oxidation state during cycling with Ca. Kuperman et al. (Kuperman et al., 2017) investigated FeHCF as a cathode material for non-aqueous calcium ion batteries and reported on the charge/discharge performances at various current densities. The authors measured reversible specific capacities ranging from 150 mAh g^{-1} (at 23 mA g^{-1}) to over 120 mAh g^{-1} (at 125 mA g^{-1}). These values were the highest storage capacities to date for a divalent calcium ion cathode for overextended cycling, and these divalent calcium ions are comparable in performance to monovalent intercalating ions.

Padigi et al. (Padigi et al., 2015a) have synthesized potassium barium hexacyanoferrate as a cathode material. The insertion/extraction of Ca^{2+} could be achieved with a reversible capacity of 55.8 mAh g^{-1} and a coulombic efficiency of 93.8%. NiHCF cathode material also featured a reversible insertion/extraction of Ca^{2+} using a Ca-based organic electrolyte (Tojo et al., 2016). A reversible capacity of about 50mAh g^{-1} was observed with coulombic efficiency of about 92%.

Aluminum Ion Batteries

CuHCF was reported as a cathode material for aqueous Al ion batteries by Gao et al (Liu et al., 2015a). The as-prepared CuHCF nanoparticles showed the ability to insert aluminum ion reversibly in aqueous solution, making it a potential cathode material for aqueous Al ion batteries. Menke et al. (Reed et al., 2015) presented reversible aluminum insertion/extraction from an organic electrolyte into CuHCF. The authors found that an aluminum-solute complex, rather than a free aluminum ion, is the exchanged species, leading to a low reversible capacity.

Other Applications

Apart from rechargeable ion batteries, PBAs can also be used as electrode materials in lithium-sulfur batteries for their abilities in adsorbing polysulfides. The unique structure of PBAs provides new possibilities in overcoming the "shuttle effect" of polysulfides, which is the main challenge in the development of Li-S batteries (Seh et al., 2016; Fang et al., 2017). Su et al. (Su et al., 2017a) reported S@PB@poly(3,4-ethylenedioxythiophene) as a cathode for lithium-sulfur batteries with a capacity of 1291 mAh g^{-1}. PB not only stores sulfur but also acts as a polysulfide diffusion inhibitor. Peng et al. (Peng et al., 2017) demonstrated that PB is effective in suppressing the shuttling of polysulfides by comparing between cathodes with and without PB.

Moreover, plenty of materials can be obtained from PBAs via thermal treatment at various conditions. Transition metal oxides are usually gained under oxidizing atmosphere, whereas metal nanoparticles@nitrogen-doped carbon frameworks are always obtained under inert atmosphere. The types and amounts of transition metals are easily regulated through compositional design of the PBA precursors. PBA-derived materials can also act as electrode materials in LIBs (Zhao et al., 2017b; Feng et al., 2016), SIBs (Chen et al., 2017a; Lim et al., 2017), lithium-air batteries (Lai et al., 2018), zinc-air batteries (Lee et al., 2016), and even Na-air/seawater batteries (Abirami et al., 2016).

Conclusions and Outlook

In this review, we introduced the recent progress in PB and its analogs in rechargeable batteries, including LIBs, SIBs, KIBs, and multivalent ion batteries. Although PBAs have been applied in energy storage for a few years and have been proved to be one of the promising electrode materials with excellent practical value, quite a few challenges such as low discharge capacity, poor cyclic stability, and low coulombic efficiency need to be addressed before their commercialization. The intrinsic performance of PBA electrodes is strongly affected by the presence of crystal imperfections such as vacancies and water molecules (including coordinated water and zeolitic water). An increase in vacancies raises the coordinated water content, which reduces redox-active sites consequently. Thus, together with the influence of zeolitic water, which also competes for interstitial sites, the initial cation content decreases.

Improved crystallinity is always a key issue in the development of PBAs. Use of complexing agents in the synthesis process may stand out from the crowd of multifarious synthesis controlling methods, considering its superiority in scale-up manufacture. Another critical challenge that PBAs faced in their commercialization is their poor electrical conductivity. Modification with different kinds of carbon materials is still the main method to overcome this problem. Multiple means of modification will be combined together in the synthesis of PBAs in the future, aiming at an all-around promotion of PBAs' electrochemical performance.

In short, PBAs are gaining more and more attention in the field of energy storage in recent years, although there is still room for improvement. We expect to spread the acquired knowledge from previous studies and hope that new ideas can help in the further development of PBAs in electrochemical energy storage.

ACKNOWLEDGMENTS

This work is supported by National Key Research and Development Program (Grant No. 2016YFB0901600), National Natural Science Foundation of China (Grant No. 51722105), Zhejiang Provincial Natural Science Foundation of China (LR18B030001), and the Fundamental Research Funds for the Central Universities (2018XZZX002-08).

AUTHOR CONTRIBUTIONS

Conceptualization, Y.J. and B.W.; writing: original draft, B.W., N.B., and X.W.; writing: review and editing, Y.J., Y.H., H.P., and M.Y.; supervision, Y.J.

REFERENCES

Abirami, M., Hwang, S.M., Yang, J., Senthilkumar, S.T., Kim, J., Go, W.S., Senthilkumar, B., Song, H.K., and Kim, Y. (2016). A metal-organic framework derived porous cobalt manganese oxide bifunctional electrocatalyst for hybrid Na-air/seawater batteries. ACS Appl. Mater. Interfaces *8*, 32778–32787.

Asakura, D., Li, C.H., Mizuno, Y., Okubo, M., Zhou, H., and Talham, D.R. (2013). Bimetallic cyanide-bridged coordination polymers as lithium ion cathode materials: core@shell nanoparticles with enhanced cyclability. J. Am. Chem. Soc. *135*, 2793–2799.

Bie, X., Kubota, K., Hosaka, T., Chihara, K., and Komaba, S. (2017). A novel K-ion battery: hexacyanoferrate(ii)/graphite cell. J. Mater. Chem. A *5*, 4325–4330.

Cai, D., Yang, X., Qu, B., and Wang, T. (2017). Comparison of the electrochemical performance of iron hexacyanoferrate with high and low quality as cathode materials for aqueous sodium-ion batteries. Chem. Commun. (Camb) *53*, 6780–6783.

Chae, M.S., Heo, J.W., Kwak, H.H., Lee, H., and Hong, S.-T. (2017a). Organic electrolyte-based rechargeable zinc-ion batteries using potassium nickel hexacyanoferrate as a cathode material. J. Power Sources *337*, 204–211.

Chae, M.S., Hyoung, J., Jang, M., Lee, H., and Hong, S.T. (2017b). Potassium nickel hexacyanoferrate as a high-voltage cathode material for nonaqueous magnesium-ion batteries. J. Power Sources *363*, 269–276.

Chen, J., Li, S., Kumar, V., and Lee, P.S. (2017a). Carbon coated bimetallic sulfide hollow nanocubes as advanced sodium ion battery anode. Adv. Energy Mater. *7*, 1700180.

Chen, L., Bao, J.L., Dong, X., Truhlar, D.G., Wang, Y., Wang, C., and Xia, Y. (2017b). Aqueous Mg-Ion battery based on polyimide anode and Prussian blue cathode. ACS Energy Lett. *2*, 1115–1121.

Chen, R., Huang, Y., Xie, M., Wang, Z., Ye, Y., Li, L., and Wu, F. (2016). Chemical inhibition method to synthesize highly crystalline Prussian blue analogs for sodium-ion battery cathodes. ACS Appl. Mater. Interfaces *8*, 31669–31676.

Chong, S., Chen, Y., Zheng, Y., Tan, Q., Shu, C., Liu, Y., and Guo, Z. (2017). Potassium ferrous ferricyanide nanoparticles as a high capacity and ultralong life cathode material for nonaqueous potassium-ion batteries. J. Mater. Chem. A *5*, 22465–22471.

Darwiche, A., Marino, C., Sougrati, M.T., Fraisse, B., Stievano, L., and Monconduit, L. (2012). Better cycling performances of bulk Sb in Na-Ion batteries compared to Li-ion systems: an unexpected electrochemical mechanism. J. Am. Chem. Soc. *134*, 20805–20811.

Dunn, B., Kamath, H., and Tarascon, J.M. (2011). Electrical energy storage for the grid: a battery of choices. Science *334*, 928–935.

Eftekhari, A. (2004). Potassium secondary cell based on Prussian blue cathode. J. Power Sources *126*, 221–228.

Eftekhari, A., Jian, Z., and Ji, X. (2017). Potassium secondary batteries. ACS Appl. Mater. Interfaces *9*, 4404–4419.

Fang, R.P., Zhao, S.Y., Sun, Z.H., Wang, W., Cheng, H.M., and Li, F. (2017). More reliable lithium-sulfur batteries: status, solutions and prospects. Adv. Mater. *29*, 1606823.

Feng, Y., Yu, X.Y., and Paik, U. (2016). Formation of Co3O4 microframes from MOFs with enhanced electrochemical performance for lithium storage and water oxidation. Chem. Commun. (Camb) *52*, 6269–6272.

Fernández-Ropero, A.J., Piernas-MuñOz, M.J., Castillo-Mart Nez, E., Rojo, T., and Casas-Cabanas, M. (2016). Electrochemical characterization of NaFe2(CN)6 Prussian blue as positive electrode for aqueous sodium-ion batteries. Electrochimica Acta *210*, 352–357.

Fu, H., Liu, C., Zhang, C., Ma, W., Wang, K., Li, Z., Lu, X., and Cao, G. (2017). Enhanced storage of sodium ions in Prussian blue cathode material through nickel doping. J. Mater. Chem. A. *5*, 9604–9610.

Ghasemi, S., Hosseini, S.R., and Asen, P. (2015). Preparation of graphene/nickel-iron hexacyanoferrate coordination polymer nanocomposite for electrochemical energy storage. Electrochim. Acta *160*, 337–346.

Guo, L., Mo, R., Shi, W., Huang, Y., Leong, Z.Y., Ding, M., Chen, F., and Yang, H.Y. (2017). A Prussian blue anode for high performance electrochemical deionization promoted by the faradaic mechanism. Nanoscale *9*, 13305–13312.

Gupta, T., Kim, A., Phadke, S., Biswas, S., Luong, T., Hertzberg, B.J., Chamoun, M., Evans-Lutterodt, K., and Steingart, D.A. (2016). Improving the cycle life of a high-rate, high-potential aqueous dual-ion battery using hyper-dendritic zinc and copper hexacyanoferrate. J. Power Sources *305*, 22–29.

He, G., and Nazar, L.F. (2017). Crystallite size control of Prussian white analogues for nonaqueous potassium-ion batteries. ACS Energy Lett. *2*, 1122–1127.

Hu, F., Li, L., and Jiang, X. (2017a). Hierarchical octahedral Na2MnFe(CN)6 and Na2MnFe(CN) 6@Ppy as cathode materials for sodium-ion batteries. Chin. J. Chem. *35*, 415–419.

Hu, Y.X., Luo, B., Ye, D.L., Zhu, X.B., Lyu, M.Q., and Wang, L.Z. (2017b). An Innovative freeze-dried reduced graphene oxide supported SnS2 cathode active material for aluminum-ion batteries. Adv. Mater. *29*, 1606132.

Hu, Y.X., Ye, D.L., Luo, B., Hu, H., Zhu, X.B., Wang, S.C., Li, L.L., Peng, S.J., and Wang, L.Z. (2018). A binder-free and free-standing cobalt Sulfide@Carbon nanotube cathode material for aluminum-ion batteries. Adv. Mater. *30*, 1703824.

Huang, Y., Xie, M., Zhang, J., Wang, Z., Jiang, Y., Xiao, G., Li, S., Li, L., Wu, F., and Chen, R. (2017). A novel border-rich Prussian blue synthetized by inhibitor control as cathode for sodium ion batteries. Nano Energy *39*, 273–283.

Hwang, J.Y., Myung, S.T., and Sun, Y.K. (2017). Sodium-ion batteries: present and future. Chem. Soc. Rev. *46*, 3529–3614.

Ji, Z., Han, B., Liang, H., Zhou, C., Gao, Q., Xia, K., and Wu, J. (2016). On the mechanism of the improved operation voltage of rhombohedral nickel hexacyanoferrate as cathodes for sodium-ion batteries. ACS Appl. Mater. Interfaces *8*, 33619–33625.

Jia, X.Q., Cai, X.J., Chen, Y., Wang, S.G., Xu, H.X., Zhang, K., Ma, M., Wu, H.X., Shi, J.L., and Chen, H.R. (2015a). Perfluoropentane-encapsulated hollow mesoporous Prussian blue nanocubes for activated ultrasound imaging and photothermal therapy of cancer. ACS Appl. Mater. Interfaces *7*, 4579–4588.

Jia, Z., Wang, B., and Wang, Y. (2015b). Copper hexacyanoferrate with a well-defined open framework as a positive electrode for aqueous zinc ion batteries. Mater. Chem. Phys. *149-150*, 601–606.

Jia, Z., Wang, J., and Wang, Y. (2014). Electrochemical sodium storage of copper hexacyanoferrate with a well-defined open framework for sodium ion batteries. RSC Adv. *4*, 22768.

Jiang, P., Shao, H., Chen, L., Feng, J., and Liu, Z. (2017a). Ion-selective copper hexacyanoferrate with an open-framework structure enables high-voltage aqueous mixed-ion batteries. J. Mater. Chem. A *5*, 16740–16747.

Jiang, X., Liu, H., Song, J., Yin, C., and Xu, H. (2016a). Hierarchical mesoporous octahedral K2Mn1−xCoxFe(CN)6as a superior cathode material for sodium-ion batteries. J. Mater. Chem. A *4*, 16205–16212.

Jiang, X., Zhang, T.R., Yang, L.Q., Li, G.C., and Lee, J.Y. (2017b). A Fe/Mn-based Prussian blue analogue as a K-rich cathode material for potassium-ion batteries. ChemElectroChem *4*, 2237–2242.

Jiang, Y., Yu, S., Wang, B., Li, Y., Sun, W., Lu, Y., Yan, M., Song, B., and Dou, S. (2016b). Prussian blue@c composite as an ultrahigh-rate and long-life sodium-ion battery cathode. Adv. Funct. Mater. *26*, 5315–5321.

Jiao, S., Tuo, J., Xie, H., Cai, Z., Wang, S., and Zhu, J. (2017). The electrochemical performance of Cu3[Fe(CN)6]2 as a cathode material for sodium-ion batteries. Mater. Res. Bull. *86*, 194–200.

Jo, I.-H., Lee, S.-M., Kim, H.-S., and Jin, B.-S. (2017). Electrochemical properties of Na x MnFe(CN) 6 · z H 2 O synthesized in a Taylor-Couette reactor as a Na-ion battery cathode material. J. Alloys Compd. *729*, 590–596.

Karyakin, A.A., Gitelmacher, O.V., and Karyakina, E.E. (1995). Prussian blue based first-generation biosensor - a sensitive amperometric electrode for glucose. Anal. Chem. *67*, 2419–2423.

Kasiri, G., Tr Coli, R., Bani Hashemi, A., and La Mantia, F. (2016). An electrochemical investigation of the aging of copper hexacyanoferrate during the operation in zinc-ion batteries. Electrochim. Acta *222*, 74–83.

Kim, D.M., Kim, Y., Arumugam, D., Woo, S.W., Jo, Y.N., Park, M.S., Kim, Y.J., Choi, N.S., and Lee, K.T. (2016). Co-intercalation of Mg(2+) and Na(+) in Na(0.69)Fe2(CN)6 as a high-voltage cathode for magnesium batteries. ACS Appl. Mater. Interfaces *8*, 8554–8560.

Kim, D.S., Zakaria, M.B., Park, M.-S., Alowasheeir, A., Alshehri, S.M., Yamauchi, Y., and Kim, H. (2017). Dual-textured Prussian blue nanocubes as sodium ion storage materials. Electrochim. Acta *240*, 300–306.

Komaba, S., Matsuura, Y., Ishikawa, T., Yabuuchi, N., Murata, W., and Kuze, S. (2012). Redox reaction of Sn-polyacrylate electrodes in aprotic Na cell. Electrochem. Commun. *21*, 65–68.

Komaba, S., Murata, W., Ishikawa, T., Yabuuchi, N., Ozeki, T., Nakayama, T., Ogata, A., Gotoh, K., and Fujiwara, K. (2011). Electrochemical Na insertion and solid electrolyte interphase for hard-carbon electrodes and application to Na-ion batteries. Adv. Funct. Mater. *21*, 3859–3867.

Kumar, A., Yusuf, S.M., and Keller, L. (2005). Structural and magnetic properties of Fe[Fe(CN)6]•4H2O. Phys. Rev. B *71*, 054414.

Kuperman, N., Padigi, P., Goncher, G., Evans, D., Thiebes, J., and Solanki, R. (2017). High performance Prussian blue cathode for nonaqueous Ca-ion intercalation battery. J. Power Sources *342*, 414–418.

Lai, Y.Q., Jiao, Y.F., Song, J.X., Zhang, K., Li, J., and Zhang, Z. (2018). Fe/Fe3C@graphitic carbon shell embedded in carbon nanotubes derived from Prussian blue as cathodes for Li-O-2 batteries. Mater. Chem. Front. *2*, 376–384.

Lee, H.W., Pasta, M., Wang, R.Y., Ruffo, R., and Cui, Y. (2014a). Effect of the alkali insertion ion on the electrochemical properties of nickel hexacyanoferrate electrodes. Faraday Discuss *176*, 69–81.

Lee, H.W., Wang, R.Y., Pasta, M., Woo Lee, S., Liu, N., and Cui, Y. (2014b). Manganese hexacyanomanganate open framework as a high-capacity positive electrode material for sodium-ion batteries. Nat. Commun. *5*, 5280.

Lee, J.-H., Ali, G., Kim, D.H., and Chung, K.Y. (2017). Metal-organic framework cathodes based on a vanadium hexacyanoferrate Prussian blue analogue for high-performance aqueous rechargeable batteries. Adv. Energy Mater. *7*, 1601491.

Lee, J.S., Nam, G., Sun, J., Higashi, S., Lee, H.W., Lee, S., Chen, W., Cui, Y., and Cho, J. (2016). Composites of a Prussian blue analogue and gelatin-derived nitrogen-doped carbon-supported porous spinel oxides as electrocatalysts for a Zn-air Battery. Adv. Energy Mater. *6*, 1601052.

Li, C., Zang, R., Li, P., Man, Z., Wang, S., Li, X., Wu, Y., Liu, S., and Wang, G. (2017a). High Crystalline Prussian white nanocubes as a promising cathode for sodium-ion batteries. Chem. Asian J. *13*, 342–349.

Li, F.F., Liu, S.Z., Cui, B.C., Lau, J., Stuart, J., Wang, B.H., and Licht, S. (2015a). A one-pot synthesis of hydrogen and carbon fuels from water and carbon dioxide. Adv. Energy Mater. *5*, 1401791.

Li, W.-J., Chou, S.-L., Wang, J.-Z., Kang, Y.-M., Wang, J.-L., Liu, Y., Gu, Q.-F., Liu, H.-K., and Dou, S.-X. (2015b). Facile method to synthesize Na-enriched Na1+xFeFe(CN)6 frameworks as cathode with superior electrochemical performance for sodium-ion batteries. Chem. Mater. *27*, 1997–2003.

Li, W.-J., Chou, S.-L., Wang, J.-Z., Wang, J.-L., Gu, Q.-F., Liu, H.-K., and Dou, S.-X. (2015c). Multifunctional conducing polymer coated Na1+xMnFe(CN)6 cathode for sodium-ion batteries with superior performance via a facile and one-step chemistry approach. Nano Energy *13*, 200–207.

Li, W., Zhang, F., Xiang, X., and Zhang, X. (2017b). Electrochemical properties and redox mechanism of Na2Ni0.4Co0.6[Fe(CN)6] nanocrystallites as high-capacity cathode for aqueous sodium-ion batteries. J. Phys. Chem. C *121*, 27805–27812.

Li, W., Zhang, F., Xiang, X., and Zhang, X. (2017c). High-efficiency Na-storage performance of a nickel-based ferricyanide cathode in high-concentration electrolytes for aqueous sodium-ion batteries. ChemElectroChem *4*, 2870–2876.

Liao, J.-Y., Hu, Q., Zou, B.-K., Xiang, J.-X., and Chen, C.-H. (2016). The role of potassium ions in iron hexacyanoferrate as a cathode material for hybrid ion batteries. Electrochim. Acta *220*, 114–121.

Lim, Y.V., Wang, Y., Kong, D., Guo, L., Wong, J.I., Ang, L.K., and Yang, H.Y. (2017). Cubic-shaped WS2 nanopetals on a Prussian blue derived nitrogen-doped carbon nanoporous framework for high performance sodium-ion batteries. J. Mater. Chem. A *5*, 10406–10415.

Lipson, A.L., Han, S.-D., Kim, S., Pan, B., Sa, N., Liao, C., Fister, T.T., Burrell, A.K., Vaughey, J.T., and Ingram, B.J. (2016). Nickel hexacyanoferrate, a versatile intercalation host for divalent ions from nonaqueous electrolytes. J. Power Sources *325*, 646–652.

Lipson, A.L., Pan, B., Lapidus, S.H., Liao, C., Vaughey, J.T., and Ingram, B.J. (2015). Rechargeable Ca-ion batteries: a new energy storage system. Chem. Mater. *27*, 8442–8447.

Liu, S., Pan, G.L., Li, G.R., and Gao, X.P. (2015a). Copper hexacyanoferrate nanoparticles as cathode material for aqueous Al-ion batteries. J. Mater. Chem. A *3*, 959–962.

Liu, Y., Qiao, Y., Zhang, W., Li, Z., Ji, X., Miao, L., Yuan, L., Hu, X., and Huang, Y. (2015b). Sodium storage in Na-rich NaxFeFe(CN)6 nanocubes. Nano Energy *12*, 386–393.

Liu, Z., Pulletikurthi, G., and Endres, F. (2016). A Prussian blue/zinc secondary battery with a bio-ionic liquid-water mixture as electrolyte. ACS Appl. Mater. Interfaces *8*, 12158–12164.

Lu, K., Song, B., Zhang, J., and Ma, H. (2016). A rechargeable Na-Zn hybrid aqueous battery fabricated with nickel hexacyanoferrate and nanostructured zinc. J. Power Sources *321*, 257–263.

Lu, Y., Wang, L., Cheng, J., and Goodenough, J.B. (2012). Prussian blue: a new framework of electrode materials for sodium batteries. Chem. Commun. (Camb) *48*, 6544–6546.

Luo, J., Sun, S., Peng, J., Liu, B., Huang, Y., Wang, K., Zhang, Q., Li, Y., Jin, Y., Liu, Y., et al. (2017). Graphene-roll-wrapped Prussian blue nanospheres as a high-performance binder-free cathode for sodium-ion batteries. ACS Appl. Mater. Interfaces *9*, 25317–25322.

Matsuda, T., Takachi, M., and Moritomo, Y. (2013). A sodium manganese ferrocyanide thin film for Na-ion batteries. Chem. Commun. (Camb) *49*, 2750–2752.

Mizuno, Y., Okubo, M., Hosono, E., Kudo, T., Oh-Ishi, K., Okazawa, A., Kojima, N., Kurono, R., Nishimura, S.-I., and Yamada, A. (2013). Electrochemical Mg2+ intercalation into a bimetallic CuFe Prussian blue analog in aqueous electrolytes. J. Mater. Chem. A *1*, 13055.

Moritomo, Y., Goto, K., and Shibata, T. (2015). Glucose-treated manganese hexacyanoferrate for sodium-ion secondary battery. Energies *8*, 9486–9494.

Moritomo, Y., Urase, S., and Shibata, T. (2016). Enhanced battery performance in manganese hexacyanoferrate by partial substitution. Electrochim. Acta *210*, 963–969.

Nakamoto, K., Sakamoto, R., Ito, M., Kitajou, A., and Okada, S. (2017). Effect of Concentrated electrolyte on aqueous sodium-ion battery with sodium manganese hexacyanoferrate cathode. Electrochemistry *85*, 179–185.

Nie, P., Shen, L., Luo, H., Ding, B., Xu, G., Wang, J., and Zhang, X. (2014). Prussian blue analogues: a new class of anode materials for lithium ion batteries. J. Mater. Chem. A. *2*, 5852–5857.

Nie, P., Shen, L., Pang, G., Zhu, Y., Xu, G., Qing, Y., Dou, H., and Zhang, X. (2015). Flexible metal–organic frameworks as superior cathodes for rechargeable sodium-ion batteries. J. Mater. Chem. A. *3*, 16590–16597.

Nie, P., Yuan, J., Wang, J., Le, Z., Xu, G., Hao, L., Pang, G., Wu, Y., Dou, H., Yan, X., and Zhang, X. (2017). Prussian blue analogue with fast kinetics through electronic coupling for sodium ion batteries. ACS Appl. Mater. Interfaces *9*, 20306–20312.

Nossol, E., Souza, V.H., and Zarbin, A.J. (2016). Carbon nanotube/Prussian blue thin films as cathodes for flexible, transparent and ITO-free potassium secondary battery. J. Colloid Interface Sci. *478*, 107–116.

Okubo, M., and Honma, I. (2013). Ternary metal Prussian blue analogue nanoparticles as cathode materials for Li-ion batteries. Dalton Trans. *42*, 15881–15884.

Oliver-Tolentino, M.A., Vazquez-Samperio, J., Cabrera-Sierra, R., and Reguera, E. (2016). Materials for aqueous sodium-ion batteries: cation mobility in a zinc hexacyanoferrate electrode. RSC Adv. *6*, 108627–108634.

Omarova, M., Koishybay, A., Yesibolati, N., Mentbayeva, A., Umirov, N., Ismailov, K., Adair, D., Babaa, M.-R., Kurmanbayeva, I., and Bakenov, Z. (2015). Nickel hexacyanoferrate nanoparticles as a low cost cathode material for lithium-ion batteries. Electrochim. Acta *184*, 58–63.

Padigi, P., Goncher, G., Evans, D., and Solanki, R. (2015a). Potassium barium hexacyanoferrate – a potential cathode material for rechargeable calcium ion batteries. J. Power Sources *273*, 460–464.

Padigi, P., Thiebes, J., Swan, M., Goncher, G., Evans, D., and Solanki, R. (2015b). Prussian green: a high rate capacity cathode for potassium ion batteries. Electrochim. Acta *166*, 32–39.

Paolella, A., Faure, C., Timoshevskii, V., Marras, S., Bertoni, G., Guerfi, A., Vijh, A., Armand, M., and Zaghib, K. (2017). A review on hexacyanoferrate-based materials for energy storage and smart windows: challenges and perspectives. J. Mater. Chem. A *5*, 18919–18932.

Pasta, M., Wang, R.Y., Ruffo, R., Qiao, R., Lee, H.-W., Shyam, B., Guo, M., Wang, Y., Wray, L.A., Yang, W., et al. (2016). Manganese–cobalt hexacyanoferrate cathodes for sodium-ion batteries. J. Mater. Chem. A *4*, 4211–4223.

Pasta, M., Wessells, C.D., Huggins, R.A., and Cui, Y. (2012). A high-rate and long cycle life aqueous electrolyte battery for grid-scale energy storage. Nat. Commun. *3*, 1149.

Pasta, M., Wessells, C.D., Liu, N., Nelson, J., Mcdowell, M.T., Huggins, R.A., Toney, M.F., and Cui, Y. (2014). Full open-framework batteries for stationary energy storage. Nat. Commun. *5*, 3007.

Paulitsch, B., Yun, J., and Bandarenka, A.S. (2017). Electrodeposited Na2VOx[Fe(CN)6] films as a cathode material for aqueous Na-ion batteries. ACS Appl. Mater. Interfaces *9*, 8107–8112.

Peng, Y.Y., Li, B., Wang, Y.H., He, X.Y., Huang, J.X., and Zhao, J.B. (2017). Prussian blue: a potential material to improve the electrochemical performance of lithium-sulfur batteries. ACS Appl. Mater. Interfaces *9*, 4397–4403.

Piernas-MuñOz, M.J., Castillo-Mart Nez, E., Bondarchuk, O., Armand, M., and Rojo, T. (2016). Higher voltage plateau cubic Prussian White for Na-ion batteries. J. Power Sources *324*, 766–773.

Piernas-MuñOz, M.J., Castillo-Mart Nez, E., Roddatis, V., Armand, M., and Rojo, T. (2014). K 1−x Fe 2+x/3 (CN) 6 · y H 2 O, Prussian blue as a displacement anode for lithium ion batteries. J. Power Sources *271*, 489–496.

Prabakar, S.J.R., Jeong, J., and Pyo, M. (2015). Highly crystalline Prussian blue/graphene composites for high-rate performance cathodes in Na-ion batteries. RSC Adv. *5*, 37545–37552.

Qian, J., Wu, C., Cao, Y., Ma, Z., Huang, Y., Ai, X., and Yang, H. (2018). Prussian blue cathode materials for sodium-ion batteries and other ion batteries. Adv. Energy Mater. https://doi.org/10.1002/aenm.201702619.

Qian, J., Wu, X., Cao, Y., Ai, X., and Yang, H. (2013). High capacity and rate capability of amorphous phosphorus for sodium ion batteries. Angew. Chem. Int. Ed. *52*, 4633–4636.

Qian, J.F., Chen, Y., Wu, L., Cao, Y.L., Ai, X.P., and Yang, H.X. (2012). High capacity Na-storage and superior cyclability of nanocomposite Sb/C anode for Na-ion batteries. Chem. Comm. *48*, 7070–7072.

Reed, L.D., Ortiz, S.N., Xiong, M., and Menke, E.J. (2015). A rechargeable aluminum-ion battery utilizing a copper hexacyanoferrate cathode in an organic electrolyte. Chem. Commun. (Camb) *51*, 14397–14400.

Ren, W., Qin, M., Zhu, Z., Yan, M., Li, Q., Zhang, L., Liu, D., and Mai, L. (2017). Activation of sodium storage sites in Prussian blue analogues via surface etching. Nano Lett. *17*, 4713–4718.

Rudola, A., Du, K., and Balaya, P. (2017). Monoclinic sodium iron hexacyanoferrate cathode and non-flammable glyme-based electrolyte for inexpensive sodium-ion batteries. J. Electrochem. Soc. *164*, A1098–A1109.

Seh, Z.W., Sun, Y.M., Zhang, Q.F., and Cui, Y. (2016). Designing high-energy lithium-sulfur batteries. Chem. Soc. Rev. *45*, 5605–5634.

Senthilkumar, S.T., Abirami, M., Kim, J., Go, W., Hwang, S.M., and Kim, Y. (2017). Sodium-ion hybrid electrolyte battery for sustainable energy storage applications. J. Power Sources *341*, 404–410.

Shen, L., Wang, Z., and Chen, L. (2014). Prussian blues as a cathode material for lithium ion batteries. Chemistry *20*, 12559–12562.

Song, J., Wang, L., Lu, Y., Liu, J., Guo, B., Xiao, P., Lee, J.J., Yang, X.Q., Henkelman, G., and Goodenough, J.B. (2015). Removal of interstitial H2O in hexacyanometallates for a superior cathode of a sodium-ion battery. J. Am. Chem. Soc. *137*, 2658–2664.

Sottmann, J., Bernal, F.L.M., Yusenko, K.V., Herrmann, M., Emerich, H., Wragg, D.S., and Margadonna, S. (2016). In operando synchrotron XRD/XAS investigation of sodium insertion into the Prussian blue analogue cathode material Na 1.32 Mn[Fe(CN) 6] 0.83 · z H 2 O. Electrochim. Acta *200*, 305–313.

Stevens, D.A., and Dahn, J.R. (2000). High capacity anode materials for rechargeable sodium-ion batteries. J. Electrochem. Soc. *147*, 1271–1273.

Su, D., Cortie, M., Fan, H., and Wang, G. (2017a). Prussian blue nanocubes with an open framework structure coated with PEDOT as high-capacity cathodes for lithium-sulfur batteries. Adv. Mater. *29*, 1700587.

Su, D., Mcdonagh, A., Qiao, S.-Z., and Wang, G. (2017b). High-capacity aqueous potassium-ion batteries for large-scale energy storage. Adv. Mater. *29*, 1604007.

Sun, X., Ji, X.-Y., Zhou, Y.-T., Shao, Y., Zang, Y., Wen, Z.-Y., and Chen, C.-H. (2016). A new gridding cyanoferrate anode material for lithium and sodium ion batteries: Ti0.75Fe0.25[Fe(CN)6] 0.96·1.9H2O with excellent electrochemical properties. J. Power Sources *314*, 35–38.

Tojo, T., Sugiura, Y., Inada, R., and Sakurai, Y. (2016). Reversible calcium ion batteries using a dehydrated Prussian blue analogue cathode. Electrochim. Acta *207*, 22–27.

Trocoli, R., and La Mantia, F. (2015). An aqueous zinc-ion battery based on copper hexacyanoferrate. ChemSusChem *8*, 481–485.

Vipin, A.K., Hu, B.Y., and Fugetsu, B. (2013). Prussian blue caged in alginate/calcium beads as adsorbents for removal of cesium ions from contaminated water. J. Hazard. Mater. *258*, 93–101.

Wan, M., Tang, Y., Wang, L., Xiang, X., Li, X., Chen, K., Xue, L., Zhang, W., and Huang, Y. (2016). Core-shell hexacyanoferrate for superior Na-ion batteries. J. Power Sources *329*, 290–296.

Wang, L., Lu, Y., Liu, J., Xu, M., Cheng, J., Zhang, D., and Goodenough, J.B. (2013a). A superior low-cost cathode for a Na-ion battery. Angew. Chem. Int. Ed. *52*, 1964–1967.

Wang, L., Song, J., Qiao, R., Wray, L.A., Hossain, M.A., Chuang, Y.D., Yang, W., Lu, Y., Evans, D., Lee, J.J., et al. (2015a). Rhombohedral Prussian white as cathode for rechargeable sodium-ion batteries. J. Am. Chem. Soc. *137*, 2548–2554.

Wang, R.Y., Shyam, B., Stone, K.H., Weker, J.N., Pasta, M., Lee, H.W., Toney, M.F., and Cui, Y. (2015b). Reversible multivalent (monovalent, divalent, trivalent) ion insertion in open framework materials. Adv. Energy Mater. *5*, 1401869.

Wang, X.-J., Krumeich, F., and Nesper, R. (2013b). Nanocomposite of manganese ferrocyanide and graphene: a promising cathode material for rechargeable lithium ion batteries. Electrochem. Commun. *34*, 246–249.

Wessells, C.D., Huggins, R.A., and Cui, Y. (2011a). Copper hexacyanoferrate battery electrodes with long cycle life and high power. Nat. Commun. *2*, 550.

Wessells, C.D., Mcdowell, M.T., Peddada, S.V., Pasta, M., Huggins, R.A., and Cui, Y. (2012). Tunable reaction potentials in open framework nanoparticle battery electrodes for grid-scale energy storage. ACS Nano *6*, 1688–1694.

Wessells, C.D., Peddada, S.V., Huggins, R.A., and Cui, Y. (2011b). Nickel hexacyanoferrate nanoparticle electrodes for aqueous sodium and potassium ion batteries. Nano Lett. *11*, 5421–5425.

Widmann, A., Kahlert, H., Petrovic-Prelevic, I., Wulff, H., Yakhmi, J.V., Bagkar, N., and Scholz, F. (2002). Structure, insertion electrochemistry, and magnetic properties of a new type of substitutional solid solutions of copper, nickel, and iron hexacyanoferrates/ hexacyanocobaltates. Inorg. Chem. *41*, 5706–5715.

Wong, M.H., Zhang, Z., Yang, X., Chen, X., and Ying, J.Y. (2015). One-pot in situ redox synthesis

of hexacyanoferrate/conductive polymer hybrids as lithium-ion battery cathodes. Chem. Commun. (Camb) *51*, 13674–13677.

Wu, J., Song, J., Dai, K., Zhuo, Z., Wray, L.A., Liu, G., Shen, Z.X., Zeng, R., Lu, Y., and Yang, W. (2017a). Modification of transition-metal redox by interstitial water in hexacyanometalate electrodes for sodium-ion batteries. J. Am. Chem. Soc. *139*, 18358–18364.

Wu, X., Deng, W., Qian, J., Cao, Y., Ai, X., and Yang, H. (2013). Single-crystal FeFe(CN)6 nanoparticles: a high capacity and high rate cathode for Na-ion batteries. J. Mater. Chem. A *1*, 10130.

Wu, X., Luo, Y., Sun, M., Qian, J., Cao, Y., Ai, X., and Yang, H. (2015a). Low-defect Prussian blue nanocubes as high capacity and long life cathodes for aqueous Na-ion batteries. Nano Energy *13*, 117–123.

Wu, X., Shao, M., Wu, C., Qian, J., Cao, Y., Ai, X., and Yang, H. (2016a). Low defect FeFe(CN)6 framework as stable host material for high performance Li-ion batteries. ACS Appl. Mater. Interfaces *8*, 23706–23712.

Wu, X., Sun, M., Guo, S., Qian, J., Liu, Y., Cao, Y., Ai, X., and Yang, H. (2015b). Vacancy-free Prussian blue nanocrystals with high capacity and superior cyclability for aqueous sodium-ion batteries. ChemNanoMat *1*, 188–193.

Wu, X., Wu, C., Wei, C., Hu, L., Qian, J., Cao, Y., Ai, X., Wang, J., and Yang, H. (2016b). Highly crystallized Na(2)CoFe(CN)(6) with suppressed lattice defects as superior cathode material for sodium-ion batteries. ACS Appl. Mater. Interfaces *8*, 5393–5399.

Wu, X.Y., Jian, Z.L., Li, Z.F., and Ji, X.L. (2017b). Prussian white analogues as promising cathode for non-aqueous potassium-ion batteries. Electrochem. Commun. *77*, 54–57.

Xie, C.-C., Yang, D.-H., Zhong, M., and Zhang, Y.-H. (2016a). Improving the performance of a ternary Prussian blue analogue as cathode of lithium battery via annealing treatment. J. Inorg. Gen. Chem. *642*, 289–293.

Xie, M., Huang, Y., Xu, M., Chen, R., Zhang, X., Li, L., and Wu, F. (2016b). Sodium titanium hexacyanoferrate as an environmentally friendly and low-cost cathode material for sodium-ion batteries. J. Power Sources *302*, 7–12.

Xie, M., Xu, M., Huang, Y., Chen, R., Zhang, X., Li, L., and Wu, F. (2015). Na2NixCo1−xFe(CN)6: a class of Prussian blue analogs with transition metal elements as cathode materials for sodium ion batteries. Electrochem. Commun. *59*, 91–94.

Xiong, P., Zeng, G., Zeng, L., and Wei, M. (2015). Prussian blue analogues Mn[Fe(CN)6] 0.6667.nH2O cubes as an anode material for lithium-ion batteries. Dalton Trans. *44*, 16746–16751.

Xu, Y., Zheng, S., Tang, H., Guo, X., Xue, H., and Pang, H. (2017). Prussian blue and its derivatives as electrode materials for electrochemical energy storage. Energy Storage Mater. *9*, 11–30.

Yagi, S., Fukuda, M., Ichitsubo, T., Nitta, K., Mizumaki, M., and Matsubara, E. (2015). EQCM analysis of redox behavior of CuFe Prussian blue analog in Mg battery electrolytes. J. Electrochem. Soc. *162*, A2356–A2361.

Yan, X., Yang, Y., Liu, E., Sun, L., Wang, H., Liao, X.-Z., He, Y., and Ma, Z.-F. (2017). Improved cycling performance of Prussian blue cathode for sodium ion batteries by controlling operation voltage range. Electrochim. Acta *225*, 235–242.

Yang, D., Xu, J., Liao, X.Z., He, Y.S., Liu, H., and Ma, Z.F. (2014). Structure optimization of Prussian blue analogue cathode materials for advanced sodium ion batteries. Chem. Commun. (Camb) *50*, 13377–13380.

Yang, D., Xu, J., Liao, X.Z., Wang, H., He, Y.S., and Ma, Z.F. (2015). Prussian blue without coordinated water as a superior cathode for sodium-ion batteries. Chem. Commun. (Camb) *51*, 8181–8184.

Ye, H., Wang, Y., Zhao, F., Huang, W., Han, N., Zhou, J., Zeng, M., and Li, Y. (2016). Iron-based sodium-ion full batteries. J. Mater. Chem. A *4*, 1754–1761.

You, Y., Wu, X.-L., Yin, Y.-X., and Guo, Y.-G. (2013). A zero-strain insertion cathode material of nickel ferricyanide for sodium-ion batteries. J. Mater. Chem. A *1*, 14061.

You, Y., Wu, X.-L., Yin, Y.-X., and Guo, Y.-G. (2014a). High-quality Prussian blue crystals as superior cathode materials for room-temperature sodium-ion batteries. Energy Environ. Sci. *7*, 1643–1647.

You, Y., Yao, H.R., Xin, S., Yin, Y.X., Zuo, T.T., Yang, C.P., Guo, Y.G., Cui, Y., Wan, L.J., and Goodenough, J.B. (2016). Subzero-temperature cathode for a sodium-ion battery. Adv. Mater. *28*, 7243–7248.

You, Y., Yu, X., Yin, Y., Nam, K.-W., and Guo, Y.-G. (2014b). Sodium iron hexacyanoferrate with high Na content as a Na-rich cathode material for Na-ion batteries. Nano Res. *8*, 117–128.

Yu, S., Li, Y., Lu, Y., Xu, B., Wang, Q., Yan, M., and Jiang, Y. (2015). A promising cathode material of sodium iron–nickel hexacyanoferrate for sodium ion batteries. J. Power Sources *275*, 45–49.

Yuan, Y., Wang, J., Hu, Z., Lei, H., Tian, D., and Jiao, S. (2016). Na 2 Co 3 [Fe(CN) 6] 2 : a promising cathode material for lithium-ion and sodium-ion batteries. J. Alloys Compd. *685*, 344–349.

Yue, Y., Binder, A.J., Guo, B., Zhang, Z., Qiao, Z.A., Tian, C., and Dai, S. (2014). Mesoporous Prussian blue analogues: template-free synthesis and sodium-ion battery applications. Angew. Chem. Int. Ed. *53*, 3134–3137.

Zhang, C., Xu, Y., Zhou, M., Liang, L., Dong, H., Wu, M., Yang, Y., and Lei, Y. (2017a). Potassium Prussian Blue nanoparticles: a low-cost cathode material for potassium-ion batteries. Adv. Funct. Mater. *27*, 1604307.

Zhang, J., Zhang, D., Niu, F., Li, X., Wang, C., and Yang, J. (2017b). FeFe(CN)6 nanocubes as a bipolar electrode material in aqueous symmetric sodium-ion batteries. ChemPlusChem *82*, 1170–1173.

Zhang, L., Chen, L., Zhou, X., and Liu, Z. (2015a). Morphology-dependent electrochemical performance of zinc hexacyanoferrate cathode for zinc-ion battery. Sci. Rep. *5*, 18263.

Zhang, L., Chen, L., Zhou, X., and Liu, Z. (2015b). Towards high-voltage aqueous metal-ion batteries beyond 1.5 V: the zinc/zinc hexacyanoferrate system. Adv. Energy Mater. *5*, 1400930.

Zhang, L., Meng, T., Mao, B., Guo, D., Qin, J., and Cao, M. (2017c). Multifunctional Prussian blue analogous@polyaniline core–shell nanocubes for lithium storage and overall water splitting. RSC Adv. *7*, 50812–50821.

Zhao, Q.X., Zhao, M.M., Qiu, J.Q., Pang, H., Lai, W.Y., and Huang, W. (2017a). Facile synthesis of Mn-3[Co(CN)(6)](2)center dot nH(2)O nanocrystals for high-performance electrochemical energy storage devices. Inorg. Chem. Front. *4*, 442–449.

Zhao, Z.W., Wen, T., Liang, K., Jiang, Y.F., Zhou, X., Shen, C.C., and Xu, A.W. (2017b). Carbon-coated Fe3O4/VOx hollow microboxes derived from metal-organic frameworks as a high-performance anode material for lithium-ion batteries. ACS Appl. Mater. Interfaces *9*, 3757–3765.